Thermal Infrared (8-13 μm) Spectra of 29 Asteroids: The Cornell Mid-Infrared Asteroid Spectroscopy ("MIDAS") Survey

Lucy F. Lim

Department of Astronomy, Cornell University, Ithaca, New York 14853

and

NASA/Goddard Space Flight Center, Greenbelt, MD 20771

lucylim@astro.cornell.edu

Timothy H. McConnochie and James F. Bell III

Department of Astronomy, Cornell University, Ithaca, New York 14853

and

Thomas L. Hayward

Gemini South Observatory, AURA/Casilla 603, La Serena, Chile

41 pages (text and references); 5 tables; 13 figures.

ABSTRACT

We report the results of the Cornell Mid-IR Asteroid Spectroscopy ("MIDAS") survey, a program of ground-based observations designed to characterize the 8-13 μm spectral properties of a statistically significant sample of asteroids from a wide variety of visible to near-IR spectral classes. MIDAS is conducted at Palomar Observatory using the Spectrocam-10 (SC-10) spectrograph on the 200-inch Hale telescope. We have measured the mid-infrared spectra of twenty-nine asteroids and have derived temperature estimates from our data that are largely consistent with the predictions of the standard thermal model. We have also generated relative emissivity spectra for the target asteroids. On only one asteroid, 1 Ceres, have we found emissivity features with spectral contrast greater than 5%. Our spectrum of 4 Vesta suggests emissivity variation at the 2-3% level. Published spectra of several of the small number of asteroids observed with ISO (six of which are also included in our survey), which appeared to exhibit much stronger emissivity features, are difficult to reconcile with our measurements. Laboratory work on mineral and meteorite samples has shown that the contrast of mid-IR spectral features is greatly reduced at fine grain sizes. Moreover, the NEAR mission found that 433 Eros is covered by a relatively thick fine-grained regolith. If small bodies in general possess such regoliths, their mid-IR spectral features may be quite subtle. This may explain the evident absence of strong emissivity variation in the majority of the MIDAS spectra.

Keywords: Asteroids, Surfaces; Spectroscopy; Infrared Observations; Asteroids, Ceres; Asteroids, Vesta

1. Introduction

Main-belt asteroids, having surface temperatures between 200 and 300 K, emit thermal radiation with spectral peaks in the 10-20 μm region. A portion of this spectral region can be observed from ground-based telescopes through the 8-13 μm atmospheric transmission window. From the disk-averaged color temperatures, constraints on the thermophysical properties of the asteroids' surface layers can be inferred. Furthermore, the silicate minerals thought to be the main constituents of asteroid surfaces have major Si-O stretching bands in the 10 μm region, and experiments have shown (*e. g.* Logan *et al.* 1973; Salisbury *et al.* 1991b) that the shapes of the emissivity spectra of laboratory samples are diagnostic of mineralogy. Certain major mineral groups, such as the plagioclase feldspars, that lack useful diagnostic features at visible to near-IR wavelengths do produce diagnostic mid-infrared features. Thermal infrared spectroscopy of asteroids, therefore, can potentially provide a considerable amount of information that is not available from other remote-sensing techniques.

Early attempts at mid-infrared asteroid spectroscopy (*e. g.* Gillett and Merrill 1975; Feierberg *et al.* 1983; Green *et al.* 1985) were hampered by a lack of understanding of the mid-infrared spectra of the calibration stars, which themselves contained substantial Si-O absorption features. (Fig. 1) The monumental work of Cohen *et al.* (10 papers, 1992-1999) in assembling accurate absolutely-calibrated spectra of mid-infrared standards made the proper calibration possible, and indeed Cohen *et al.* themselves soon published 5-14 μm Kuiper Airborne Observatory (KAO) spectra of 1 Ceres, 2 Pallas and 4 Vesta (Cohen *et al.* 1998; Witteborn *et al.* 1999), with spectral uncertainties of 10-20%. Space-based 6-12 μm asteroid spectra from the ESA Infrared Space Observatory (ISO) were published by Dotto *et al.* (2000); Barucci *et al.* (2002); and Dotto *et al.* (2002), who concluded from their observations that they had detected

mineralogical spectral emissivity variations; and by Mueller and Blommaert (2004). Again, however, only a handful of the brightest main-belt asteroids were covered.

Here we present the results of the Cornell Mid-Infrared Asteroid Spectroscopy ("MIDAS") Survey: ground-based mid-IR spectra of twenty-nine asteroids measured with Spectrocam-10 on the 200" Hale telescope at Palomar Observatory and calibrated on the standard stars of Cohen *et al.* Our uncertainties in absolute flux are approximately 10% for all our data, with spectral uncertainties ranging from 2-5%. We have attempted to represent the widest possible variety of the traditional visible-to near- IR spectral classes in our target sample. Using a simple thermal model, we have estimated the sizes and surface temperatures of the asteroids in our survey. For two asteroids, 1 Ceres and 4 Vesta, we detect spectral emissivity variation that is likely to be mineralogical in origin. We rule out emissivity variation at the 5% level for the remaining twenty-seven asteroids.

2. Observations

We observed twenty-nine asteroids over the course of three observing runs: October 2-3 (UT), 2001, September 21-22, 2002, and August 22-23, 2003. The circumstances of our observations are given as Table 1. All our spectra were taken with Spectrocam-10 on the 200" Hale telescope at Palomar Observatory. The design of Spectrocam-10 (SC-10) is described in detail in Hayward *et al.* (1993); what follows here is a brief overview.

Spectrocam-10 is a combination camera and long-slit spectrograph designed to operate in the 8-13 μm atmospheric window. It is mounted at the Cassegrain focus of the 200" telescope in a liquid nitrogen cooled dewar. The detector and filter wheel are cooled further in a second, liquid-helium-filled dewar. A pickoff mirror directs the

beam from the telescope's secondary into the dewar; from there, two spherical mirrors refocus the beam and direct it through one of several available slits (mounted on a slit wheel). A paraboloidal mirror then collimates the beam and reflects it to a grating scan mechanism, which can either disperse the collimated beam using one of two gratings in the spectrograph modes, or reflect it with an optical flat for camera mode. The beam then returns to the paraboloidal mirror, which focuses it through a filter wheel and onto the detector. The detector itself is an arsenic-doped silicon (Si:As) BIBIB (Back Illuminated Blocked Impurity Band) array of 128 x 128 elements.

Because the mineralogical features of interest to us are relatively broad in wavelength and hence do not require high spectral resolution, we used the low-resolution mode and wide $2''$ slit exclusively in order to maximize our signal to noise ratio and spectral coverage. The nominal noise equivalent flux density (NEFD) for a 100s exposure in low-resolution mode is 25 mJy ($7.5 \cdot 10^{-16}$ W/m^2/μm). (For comparison, the faintest of our asteroid targets were approximately $2 \cdot 10^{-13}$ W/m^2/μm at 10 μm.) The dispersion in low-resolution mode is 0.024 μm/pixel; consequently not more than three μm of a spectrum can fit on the 128-pixel detector at one time. Moreover, due to vignetting and "rolloff" in detector sensitivity near the edges of the chip, the actual usable range is restricted to about 2.8 μm. To cover the 8-14 μm window, we took three overlapping spectral segments with the grating scan mechanism in different positions, centered at wavelengths of 9.2, 10.7, and 12.2 μm.

The grating scan mechanism (GSM) is designed to move the diffraction gratings and optical flat in and out of place to switch instrument modes and to rotate the gratings to cover different wavelength regions within each mode. Because it is mobile, and because it has to be moved frequently when the instrument is in use, it is less stable than the fixed optical components of SC-10. Although it is equipped with a heater and thermostat to reduce instability due to temperature changes over the course of

the night, we found that we had to be vigilant about checking and adjusting the GSM position after each spectral segment. Some detectable drift nevertheless remained, which led to offsets from one spectrum to another in the wavelength registration on the chip. These offsets were usually subpixel, but could occasionally be as large as 1-2 pixels, as we found when we calibrated the raw spectra in wavelength using telluric atmospheric features. Our wavelength registration procedure is discussed more thoroughly in "Calibration and Processing." The standard deviation of the wavelength of any given pixel over a single night was typically about 0.02 μm; the detector spectral scale was 0.0232 μm/pixel.

At mid-infrared wavelengths, both the sky and the telescope itself emit their own thermal radiation and are bright with respect to the target objects. In order to enable accurate subtraction of this background radiation, spectra of the empty sky adjacent to the astronomical target must be measured. The rapidly varying sky background is measured by moving, or "chopping," the secondary mirror between on-target and off-target beams at a high frequency. In our observations, we chopped three times per second. The chip itself is read out faster still in order to avoid filling the detector wells beyond their linear range. Each of these images is known as a "frame", so that in our data SC-10 has read the detector out at eight frames per chop, or 24 times per second. The frames belonging to each chop position are co-added by SC-10 in two hardware memory buffers, so that the instrument does not output every frame individually, but only one co-added image per chop position.

We chose our readout frequency carefully to keep the detector in its linear range throughout. The detector was brightest around $\lambda = 12$ μm due to emission from a set of terrestrial water lines and reached 1200-1300 mV; it was darkest in the region at the extreme short end of our spectral range, and the detector output was approximately 100 mV at $\lambda = 8$ μm.

The variation in the light path through the telescope between chop positions is compensated for by moving the entire telescope to take spectra of the target and sky in both chop positions ("nodding"). A minimal complete measurement must therefore include four raw spectral images or "beams", one for each permutation of chop and nod positions.

Spectrocam-10's field of view is 64 pixels wide ($16''$) in the spatial direction; wide enough that it was possible to chop and nod "on-chip", so that the dispersed image of the star or asteroid could be included in all four beams of the sequence, as illustrated in Fig. 2. In each beam the dispersed image falls on a different row of the detector. The background subtraction then yielded a combination image (Fig. 2c) containing two positive and two negative dispersed images of the target, parallel to each other and centered on various rows of the detector. The rows containing these images were automatically identified and added together with the appropriate sign changes to produce a segment of the asteroid's spectrum.

Our measurements typically consisted of four or eight beams (one or two complete sets taken consecutively) of twenty seconds each, and since the source was always on-chip, the total integration time per spectral segment was 80 seconds for a four-beam measurement or 160 seconds for an eight-beam segment.

The resulting spectral segment represented the flux spectrum of the target asteroid convolved with the atmospheric transmission and instrumental response functions. In order to isolate the asteroid's spectrum, we needed to estimate the overall response function by measuring the spectrum of a mid-infrared calibration standard under similar atmospheric conditions. For each asteroid spectrum, therefore, we planned a corresponding observation of a standard star as close to the asteroid data as possible in time and airmass. Our standards needed to be bright stars whose true infrared spectra were well known. Whenever possible, we used the observed composite spectra

compiled by Cohen *et al.* (1992, 1999) for six of their "primary standards": α Ceti, α Lyrae, α Tauri, β Andromedae, β Geminorum, and β Pegasi. However, because a number of our target asteroids were far from all of these stars in the sky at the time we observed them, in several cases we were obliged to use other bright mid-infrared stars – most notably, γ Aquilae (HD 186791), for which Cohen *et al.* published a template file based on the spectrum of a star of similar spectral type (α Hydrae) but no observed spectra (Fig. 3). In these cases, we had to flux calibrate these stars on the primary standards before using their spectra to calibrate the asteroid spectra, thereby adding another level of atmospheric uncertainty to our results. In the case of γ Aquilae, we averaged three spectra, two calibrated on α Lyrae and one on β Pegasi, to produce the spectrum illustrated in Fig. 3. Slight changes in the atmospheric transmission between the times of the asteroid and standard observations remain one of our primary sources of uncertainty.

3.   Calibration and Processing

Each of our spectra was assembled from three overlapping spectral segments. In the raw dispersed images, the short-wavelength segment ranged from 7.6 to 10.6 μm; the medium, from 9.2 to 12.2 μm; and the long, from 10.7 to 13.7 μm. Because of "rolloff" in the detector's sensitivity close to its edges and low atmospheric transmission below 8.2 μm and above 13.2 μm, the ranges of the usable portions of the segments were 8.2 to 10.4 μm, 9.3 to 12.0 μm, and 10.9 to 13.2 μm respectively.

We extracted spectral segments from the dispersed images. Due to the on-chip chopping and nodding, each two-dimensional image contained four parallel dispersed images of the target asteroid or standard (see Fig. 2a): two positive images superimposed on each other along the central row of the detector (close to row 32) and two negative flanking images centered near rows 16 and 48. The dispersion was very nearly parallel to the

rows of the detector array, so that the central row for any given image at column 0 of the detector was consistently less than half a pixel removed from its central row at column 127. We located the precise centers of the images by fitting a function composed of a Gaussian flanked by two half-strength Gaussians of opposite sign to each column. The centers, amplitudes, and widths (related to the seeing and telescope tracking) of the Gaussians were permitted to float. The medians of the three resulting sets of central rows were taken to be the true central rows of the images, and the medians of the sets of widths were taken to be the true width of the point spread function. The rows within 3σ of the three central rows were summed to produce three one-dimensional spectral segments, one positive and two negative, with the maximum ratio of signal to noise. An example of the overall pre-extraction spatial profile of an SC-10 segment is included as Fig. 2b; the corresponding two-dimensional detector image is Fig. 2c.

No spectral errors were introduced by this profile extraction, since the spatial profile did not change as a function of wavelength, and the same rows of pixels were summed from one end of the detector to the other.

The chop direction was at a very small angle to the column direction of the detector, so that we had to offset the flanking images in column number slightly before adding them to the central image. We measured these offsets by calculating the wavelength calibration for all of the central and flanking images separately and averaging. Since the offset angle did not change during any given night, the average wavelength offset would be more accurate than the result of any individual wavelength calibration. Without this correction, the wavelength resolution of the spectral segments would have been degraded slightly.

The segments from the two negative flanking images were reversed in sign before the three segments were added together, so that the total result from the two-dimensional chopped and nodded detector output was one one-dimensional spectral segment.

Before we could combine the asteroid and standard spectral segments into a single spectrum calibrated in flux, we had to calibrate them in wavelength.

The prominent telluric lines in each spectral segment provided convenient reference points for wavelength calibration (see for example Lord 1992 for the wavelengths of various telluric absorption features). In the short- and medium- wavelength segments, we relied on the ozone absorption structures centered around 9.49 and 9.648 μm. In the long-wavelength segments, we used the 12.55 μm water vapor feature.

In order to calibrate our standard star data, we created a reference spectrum by multiplying the model spectrum of the star (Cohen *et al.* 1999) by a standard model of atmospheric transmissivity (Fig. 4) and reducing the spectral resolution appropriately. We compared a segment of this model that included the telluric feature to be used for calibration with the standard star data containing the same feature. We first "rebinned" the 128-pixel array onto a wavelength scale with three times as many array elements in wavelength as the detector, so that we could conveniently make subpixel adjustments to the registration by integer numbers of array elements. We then adjusted the wavelength registration for our data until we had maximized the correlation between the data and the model.

We followed a similar procedure to register the asteroid spectra in wavelength, except that in place of the standard atmosphere we used the transmissivity function derived from the calibrated standard star spectrum. We multiplied the derived transmissivity by a standard thermal model (spherical greybody) spectrum of the asteroid to produce our theoretical reference spectrum. The standard thermal model will be discussed more thoroughly in Section 5.

The results of these automated calibrations were plotted together with their ratio and examined by hand. The telluric lines are strong and steeply sloped, so that a small offset in the wavelength registration could produce a prominent artifact in the

ratio of asteroid to standard data. When it was necessary, we adjusted the result of our automated wavelength registration routines manually until these artifacts were minimized. This process is illustrated in Fig. 5. These manual adjustments were never greater than 2/3 of a detector pixel, or 0.016 μm.

Once the standard star's spectrum had been calibrated in wavelength, the ratio of the measured spectrum to the true spectrum of the calibrator (Cohen *et al.* 1999) represented a combination of the atmospheric transmission function and the efficiency of Spectrocam-10 at the time and airmass of the calibration data. In the cases where our asteroid and standard data were separated by more than 0.1 airmasses, we applied an airmass correction consisting of the ratio of the transmission through a model atmosphere (from the "ATRAN" program for Palomar, Lord 1992) at the asteroid's airmass to the transmission through the same model atmosphere at the standard star's airmass. The measured spectral segments from the target asteroid could then be divided by the corrected transmission function to yield the true flux spectrum of the asteroid in three segments.

Because of slit losses and atmospheric instability (largely water vapor variations), the spectral segments were sometimes offset in overall flux and had to be scaled before they could be combined into a single spectrum. In these cases, we scaled the short- and long- wavelength segments to the 9.4-11.5 μm segment by the ratio of the medians of their fluxes in the overlapping regions. We spliced the three segments together to form the complete 8.2-13.2 μm spectrum of the asteroid. The overlapping regions of the resulting spectra therefore represent twice as much integration time as the nonoverlapping regions.

4. Sources of Uncertainty

Our spectra have two types of uncertainty: uncertainty in the overall flux, or global uncertainty; and point-to-point uncertainty in the spectral shape, or local uncertainty. The global uncertainties affect only the radius estimates of our asteroids, while the local uncertainties affect the subsolar temperature estimates and the shapes of the emissivity spectra.

The principal sources of global uncertainties are slit losses, which varied from segment to segment due to changes in the seeing and imperfect telescope tracking; atmospheric changes between the time when the standard star was measured and the time when the asteroid was measured; and global uncertainty in the reference spectra of the standard stars. The latter have been published by Cohen *et al.*, who assign "global bias"[1] values of 1.45% to their reference spectra of β Pegasi, α Tauri, β Geminorum, and β Andromedae; 1.46% for α Lyrae and α Ceti; 5% to 7.5% for their "template" spectrum of γ Aquilae; and 2.5% for their template spectrum of η Ceti. Our total global flux uncertainty can be estimated by comparing airmass-corrected calibration star spectra taken at various times during our observations with each other. We assign a uniform value of 10% uncertainty in global flux to all our data. Note that this uncertainty in the overall flux is much larger than the local uncertainties in the emissivity spectra of the asteroids, which are represented by the point-to-point scatter in the spectra.

The sources of local uncertainty are atmospheric variations, statistical photon noise, and local uncertainties in the reference spectra of the standard stars. In cases where the standard spectrum had to be corrected to the airmass of the asteroid spectrum, deviation of the actual atmospheric transmission from the model atmospheric profile used in the airmass correction is also a source of local uncertainty. Finally, imperfect

---

[1]Cohen *et al.* use the term "global bias" to refer to the overall flux uncertainty, which does not contribute error to spectral shape or color measurements.

wavelength calibration can create substantial artifacts in the emissivity spectrum (see Fig. 5), particularly close to major telluric lines.

Because the mineralogical emissivity features in this spectral region are quite broad in wavelength, extending over 0.5 μm or more (Fig. 6), we resampled our spectra into 0.1-μm bins, which each corresponded to just over four SC-10 pixels. We then used the standard deviation among the points in each bin in order to estimate our local uncertainties.

5.   Radius and temperature fits: the standard thermal model

We fit our data to the asteroid standard thermal model (STM). The STM (Lebofsky and Spencer 1989) models the asteroids as spheres of uniform emissivity in instantaneous thermal equilibrium with the incident solar radiation. The model spectrum, therefore, has only two parameters: a scaling factor that depends on the radius of the asteroid and asteroid-Earth distance, and the temperature of the asteroid's surface at the subsolar point. We allowed both of these quantities to vary during our χ^2 fitting. The surface temperatures at all other points on the asteroid can be expressed simply in terms of the temperature at the subsolar point:

$$T(\theta) = T_{subsolar} cos^{\frac{1}{4}}(\theta) \tag{1}$$

The STM spectrum is always calculated for a solar phase angle of zero, then corrected for phase by 0.01 magnitudes/degree (with uncertainties of +0.007 to -0.005) of phase, based on mid-infrared photometry by Matson (1971b) of main-belt asteroids at a variety of phase angles. Since this correction is not wavelength-dependent, this phase correction does not produce any change in the shape of the model spectrum, and

therefore does not affect the temperature determinations. Its uncertainties have been incorporated, in a root-summed-square sense, into the uncertainties quoted for our radius estimates.

The subsolar point temperature is a function of the asteroid-Sun distance, asteroid bolometric albedo, and asteroid effective emissivity. In the STM, it is also affected by an empirical factor known as the "beaming parameter", which represents a combination of other thermophysical properties of the surface layer. The most important of these is preferential beaming of thermal radiation in the sunward direction due to surface roughness: the floors of craters, for instance, will receive reflected and emitted radiation from the illuminated crater walls in addition to the direct insolation. A "beaming parameter" less than unity will increase the predicted subsolar point temperature, so that

$$T_{subsolar} = \left[\frac{(1 - albedo)(insolation)}{\eta \epsilon \sigma} \right]^{\frac{1}{4}} \qquad (2)$$

where η represents the beaming parameter, ϵ the emissivity, and σ the Stefan-Boltzmann constant.

The insolation is a straightforward inverse-square function of the asteroid-Sun distance, which for each of our targets was readily available from JPL "Horizons" (horizons.jpl.nasa.gov, Giorgini *et al.* (1996)). Our temperature measurement therefore constrains $(1 - albedo)/(\eta \cdot \epsilon_{effective})$ for the target asteroid. A higher albedo leads to a lower temperature because less of the insolation is absorbed. A higher effective emissivity also produces a lower temperature because the asteroid is able to re-radiate its energy more efficiently.

In Table 2 (STM Temperature and Radius Fits), the "predicted subsolar temperatures" were calculated from Eq. 2 with a value of 0.756 for the beaming parameter (Lebofsky

et al. 1986). This value was derived empirically from radiometry of 1 Ceres and 2 Pallas (see Spencer *et al.* (1989), Table II, and references therein), whose diameters were known independently from occultation data. It carries an uncertainty of $\pm$ 0.014, which corresponds to $\pm$ 1.3 K at an asteroid-Sun distance of 2 AU. (However, compare Harris (1998), who argues that for near-Earth asteroids the appropriate values of η may be much higher, and suggests a default value of η = 1.2.) The earlier radiometric asteroid diameters of the IRAS Minor Planet Survey (IMPS) (Matson 1986; Tedesco 1989; Tedesco *et al.* 2002) were derived by applying this canonical value to IRAS radiometry. In contrast, using MIDAS spectral data, we can measure color temperature and fit η independently for each asteroid. This is essentially the same method employed by Harris (1998) using thermal infrared spectrophotometry.

We used two values for effective emissivity: 0.98 for low-albedo objects (p $\leqq$ 0.11) and M-class asteroids and 0.95 for higher-albedo asteroids. These estimates are based on laboratory spectra measured by Salisbury *et al.* (1991a) for powdered samples of carbonaceous and ordinary chondrites respectively, translated to emissivity (see footnote 7 under "Interpretation") and averaged over the spectral region between 8 and 20 μm, where main-belt asteroids emit most of their thermal radiation[2]. Altering the model emissivity by 3% changes the predicted subsolar temperature by 2 K.

A departure from this "STM predicted temperature" in our χ^2 fitting implies either that the asteroid's surface differs in bolometric albedo from the albedo used to predict the temperature, or that the asteroid's effective emissivity or other thermal properties (represented by the beaming parameter) differ from those of Ceres and Pallas. The uncertainties in our temperature measurements themselves, cited in Table 2, are the formal errors from the χ^2 temperature fits (Bevington and Robinson 1992, p. 147).

---

[2]A value of 0.90 for "silicate emissivity" is often used in the literature, but is more appropriate for warmer objects where a substantial portion of the thermal radiation is emitted shortward of 8 μm.

Only data between 8.2 and 13.2 μm were used in these fits; we also excluded data points that fell within the highly variable telluric ozone structure (9.25 to 10.2 μm). It is worth noting that these temperature measurements are unaffected by global flux uncertainties caused by slit losses, for example, and can only be affected by spectral errors.

6. Results

The flux spectra for our twenty-nine asteroid targets are plotted as Fig. 7. The error bars in these plots represent spectral uncertainties only, and are derived from the scatter of points within each 0.1-μm wavelength bin. The best-fit STM model spectra are overplotted as dashed lines. The vertical grey bars in the background mark the locations of prominent telluric atmospheric features (see also Fig. 4) where the systematic errors for the data points may be much larger than the formal error bars.

Consecutive measurements have generally been averaged together and presented as a single spectrum, both in Figs. 7 and 8 and in Tables 1 and 2. However, for a number of asteroids which were measured on more than one night, or at several substantially different times on the same night, we have presented several separate spectra of a single asteroid.

The early part of the night on 2 October 2001 was generally non-photometric due to cirrus, and we consider the absolute flux measurements and emissivity spectra from 2 October less reliable than the majority of our data. During our other three nights of observations (3 October 2001, 21 September 2002, 22 September 2002) we enjoyed excellent observing conditions, and our flux errors were limited by variations in slit losses. Based on repeated observations of standard stars, we estimate a constant flux uncertainty of 10%, which contributes 5% to the uncertainty in the asteroid

radius. This 5% is combined with the uncertainties in the phase corrections in a root-sum-square sense to produce the total radius uncertainties quoted in Table 2.

These radius uncertainties represent only the component of radius uncertainty that is independent of the temperature estimate; that is, the amount of uncertainty that would remain in the radius if there were zero uncertainty in the temperature distribution on the asteroid surface. The radius estimates are also dependent on the temperatures we estimate for the subsolar point. Thus, for example, for our spectrum of 24 Themis the least-squares fit is [$T_{subsolar}$ = 230.6 K, radius = 105 km], but if the subsolar temperature is decreased by one standard deviation to 226.6 K, the model radius must be increased to produce the observed flux, so that the best fit at the lower temperature is [$T_{subsolar}$ = 226.6 K, radius = 110.5 km]. Other potential sources of error, such as shape irregularity, are also not represented in Table 2.

The emissivity spectrum of an asteroid is the ratio of the measured spectrum of the asteroid to the fitted STM spectrum. In the majority of cases, the asteroid spectra we observed were without spectral emissivity variation to within 5%, and were good matches to the STM with a beaming parameter (η) of 0.756 ± 0.014. Note that although an incorrect STM spectrum can change the overall slope of the emissivity spectrum, it can neither hide the relatively narrow mineralogical features nor produce spurious features, so that these results are not vulnerable to errors in thermal modelling. We have plotted relative emissivity as a function of wavelength for 1 Ceres, 2 Pallas, 3 Juno, 4 Vesta, 10 Hygiea, and 511 Davida as Fig. 8, and we discuss these and other asteroids individually below.[3]

_____

[3]All the data published in this paper are available in digital form from the author on request.

7. Discussions of Individual Asteroids

7.1. 1 Ceres

By far the largest spectral emissivity variations in our data are to be found in the spectrum of 1 Ceres, which has a 10% increase in emissivity between 8.7 and 9.6 μm together with a more gradual decrease in emissivity longward of 10.8 μm to about 11.6 μm. The precise rollover wavelength is obscured by telluric ozone absorption. This feature was reproducible in two spectra taken on 21 September and one on 22 September 2002. We have plotted our spectra in flux in Fig. 7, and divided them by the best-fit STM model to produce the relative emittance spectra shown in Fig. 8. Our spectra essentially reproduce those published by Cohen *et al.* (1998) from KAO data and by Dotto *et al.* (2000) from ISO PHT-S data.

Our subsolar temperature estimates agree very well with the STM temperature predictions for 11% albedo and 98% effective emissivity. We find $T_{subsolar} = 242 \pm 1$ K for both nights. The STM subsolar temperature prediction was 242.4 K.

We derived radii R = 471 $\pm$ 25 km, 468 $\pm$ 25 km (21 and 22 September respectively). These are consistent with several other estimates of the size of Ceres: Millis *et al.* (1987) derived occultation radii of 479.6 $\pm$ 2.4 km (equatorial) and 453.4 $\pm$ 4.5 km (polar), and the radiometric IRAS Minor Planet Survey (IMPS) radius (Tedesco 1989) was 457 $\pm$ 22 km.[4] More recently, Parker *et al.* (2002) have used Hubble Space Telescope (HST)

---

[4]Tedesco *et al.* (2002) revised the original IMPS diameters for all asteroids observed by IRAS, including Ceres, with a "band-to-band correction" that improved the consistency between the albedos derived from the various IRAS wavelengths (12, 25, and 60 μm) for most asteroids. Their revised estimate for Ceres' radius was 424.2 $\pm$ 9.9 km, which is, of course, well below both our estimate and the occultation and HST-derived values. However, the authors acknowledged that for the largest asteroids, including Ceres, this correction produced diameters that were systematically low compared to occultation-derived diameters. The original calibration had been based on observations of Ceres itself and of 2 Pallas. Tedesco *et al.* suggested that this discrepancy might be explained if very large asteroids (D $\gg$ 200 km) had atypical thermal properties. We will continue to cite, when appropriate, both the original and revised IMPS diameters in this paper.

data to find the semimajor and semiminor axes of Ceres: 484 ± 5.1 km and 466.4 ± 5.9 km respectively, with an equivalent radius R = 475.5 ± 3.9 km.

Cohen *et al.* (1998) devoted several pages to the mineralogy of Ceres but were unable to match its spectrum either with the silicate samples of Salisbury *et al.* (1991b), the powdered Murchison meteorite, the ammoniated phyllosilicates of King *et al.* (1992), or the organic materials supplied by Calvin (1997, cited as a private communication by Cohen *et al.*). They suggested that a finer grain size of the organic tholin, mixed with a higher-emissivity material, might produce a closer match; but such a laboratory measurement was not available. Dotto *et al.* (2000) also attempted to compare their spectrum with several laboratory samples, including a mica and an oxide mineral, but did not find any compelling matches.

7.2.   2 Pallas

We measured 2 Pallas on October 3, 2001, September 22, 2002, August 21, 2003, and August 22, 2003. Unfortunately, in the first two cases we were obliged to calibrate our spectra on γ Aquilae (see Fig. 4) instead of directly on a primary standard of Cohen, so that our calibrated spectra include two layers of atmospheric uncertainty. Nevertheless, our radius and temperature fitting results do agree with the STM predicted temperatures and 266 ± 3 km occultation radius (Dunham *et al.* 1990). All of our spectra are within their 2-5% error bars of uniform emissivity. Dotto *et al.* (2000) reported an ISO spectrum of 2 Pallas with an emissivity maximum of 8-10% spectral contrast, centered around 10.5 μm in wavelength and about one μm in breadth. They noted that this structure was consistent with water ice. Within the limits of our error bars, we see no convincing evidence for this feature or any other in our data.

7.3. 3 Juno

We measured 3 Juno under marginal observing conditions on October 2, 2001. These observations also suffer from a high airmass contrast between the asteroid (1.26 airmasses) and standard star (β Geminorum at 1.07 airmasses). The small emissivity maximum at 11.85 μm and minimum at 12.4 μm are therefore likely to be spurious features resulting from the nearby telluric absorption bands. We measure a subsolar temperature of 293 ± 7 K and a radius of 136 ± 11 km.

Our radius agrees with the occultation-derived radius of Millis *et al.* (1981) (D = 267 $\pm$ 5 km, or R = 133.5 ± 2.5 km), rather than with the revised IMPS radius of 117 km.

Our subsolar temperature measurement of 293 ± 7 K is much higher than the STM would predict based on an albedo of 0.24 (Tedesco *et al.* 2002). However, Morrison (1974) published a radiometrically determined bolometric albedo of 0.15 for 3 Juno, which yields a predicted subsolar temperature (284.6 K) close to the lower limit of our error bars. If we assume a subsolar temperature of 285 K, our data are consistent with a radius of 144 ± 11 km.

Dotto *et al.* also measured this asteroid with ISO. Their data, which cover the wavelength range 5.8-11.6 μm, are consistent with a flat spectrum between 8.6 and 11.5 μm with decreased emissivity shortward of 8.6 μm, as are ours. Dotto *et al.* argue that this structure is a Christiansen peak located at about 8.6 μm and suggest that it is diagnostic of a pyroxene/olivine surface composition.

7.4. 4 Vesta

The ISO spectrum of 4 Vesta presented by Dotto *et al.* (2000) showed strong features: a positive slope from 8.2 to 9.1 μm with about 10% overall contrast and an absorption

feature centered around 10 μm, also with about 10% contrast. These features are absent from our spectra of 4 Vesta.

We measured Vesta repeatedly on two consecutive nights in 2001, for a total of 640 seconds per segment on October 2 and 320 seconds on October 3.[5]

Due to atmospheric stability, the brightness of the asteroid, and the close proximity in the sky of a bright and well-characterized mid-infrared standard (α Tauri), we were able to obtain local uncertainties of less than 2%. These spectra are plotted in flux in Fig. 7 and in emissivity in Fig. 8, and represent our best data.

We divided the flux spectra by the best-fit STM models and averaged the spectra from each night together in order to obtain the emissivity spectra shown in Fig. 8 and Fig. 9. On both nights, we observed a negative slope between 8.3 and 9.1 μm of 3-4% overall contrast, a small distinct peak in emissivity around 11 μm, and a positive slope between 12.3 and 13.1 μm of about 3% contrast. No feature had a spectral contrast of more than 4%. These are at best marginal detections, and we have not attempted a mineralogical analysis. We note, however, that several of these features can also be found in the spectra of certain HED meteorites, as measured by Salisbury *et al.* (1991a) (Fig. 9).

The pole and rotation period of Vesta have been well established (Thomas *et al.* 1997; Drummond *et al.* 1998) with an uncertainty of 5° in the pole orientation. Using the Thomas *et al.* pole solution (RA = 301°, Dec = 41°; prime meridian = 292° + 1617.332776 °/day · (Julian Date - 2451545.0)) we can estimate our fields of view on the asteroid from the two nights of observations. Since in the standard thermal model

---

[5]Our second set of observations on October 2 appear to have been plagued by slit losses due to imperfect tracking on the asteroid. Since the shape of the spectrum does not seem to have been affected, we have averaged all the Oct. 2 data (640 s) for the emissivity spectrum in Fig. 8 but only the first set of observations for the flux spectrum in Fig. 7. The following night we were more vigilant about monitoring the instrument and experienced no such problems.

98% of the flux comes from within 70° of the sub-observation point, we have mapped these seventy-degree fields of view for the sub-Earth points at the times of the MIDAS and ISO observations onto a simple cylindrical projection of Vesta in Fig. 10. Based on this map, it is possible though perhaps unlikely that the differences between our spectra and ISO's could be explained in terms of a strategically-placed terrain with a strong spectral signature.

Our temperature fits for Vesta's subsolar point are 251 ± 1 K and 247 ± 1 K for the spectra measured on October 2 and October 3 respectively. The IMPS (Tedesco *et al.* 2002) reports a visible geometric albedo of 0.42 ± 0.05 for this asteroid, which if adopted as a bolometric albedo leads to a prediction of 231.8 K for the subsolar point using an emissivity of 0.95 (consistent with the laboratory measurements by Salisbury *et al.* of HED meteorites) and standard beaming parameter of 0.756. However, in Table 2 we have cited the more plausible bolometric geometric albedo of Morrison (1974), which is 0.24, and its corresponding temperature prediction of 250 K.

Our radius estimates for Vesta were 263 ± 19 km and 256 ± 18 km, which are entirely consistent with other data: Thomas *et al.* (1997) model the asteroid's shape using HST data as a nearly-ellipsoidal object with radii of 289, 280, and 229 ± 5 km, with a mean radius of 265 km.

7.5. 10 Hygiea

Barucci *et al.* (2002) have published an ISO spectrum of 10 Hygiea that contains another feature of approximately 10% spectral contrast: a region of increased emissivity between about 9.4 and 11.4 μm. We measured 10 Hygiea on three separate nights with SC-10: once in October 2001 and twice on consecutive nights in September 2002, for a total of about eight hundred seconds of integration time per spectral segment. In none

of these spectra do we observe a feature similar to that reported by Barucci *et al.*, or indeed any features at all; all three spectra are remarkably good fits to a smooth STM spectrum. The spectra are plotted in flux in Fig. 7 and in emissivity in Fig. 8.

The sub-Earth points of these observations were not identical with those of the ISO measurements. However, Barucci *et al.* (2002) report this feature in two separate spectra taken with different ISO instruments (PHT-S and SWS) at different times.

Two possible solutions for the spin vector of Hygiea have been found by a number of investigators (see Lopez-Gonzalez and Rodriguez (2000), Erikson and Magnusson (1993), and Michalowski *et al.* (1991)) to be consistent with lightcurves measured between 1953 and 1996. Using each of these pole determinations and a rotation period of 1.150967 days (Magnusson *et al.* 1993), we have mapped the seventy-degree fields of view of the five observations (two ISO and three MIDAS spectra) as Figs. 11a and 11b. We defined meridians to coincide with one of the lightcurve minima for each pole solution: W = 147.4°- 312.78047°/day · (Julian Date - 2451545.0) for the "p3" solution and W = 350.54°- 312.78047°/day · (Julian Date - 2451545.0) for the "p4" solution.

If the "p4" pole solution is correct, the fields of view of the ISO PHT-S and SWS measurements on the asteroid did not overlap, although each had some area in common with the MIDAS coverage. Therefore, in order to explain the discrepancy between the two ISO spectra and the MIDAS data in terms of surface variations on 10 Hygiea, it would be necessary to assume that at least two separate facets of the asteroid are occupied by a terrain with a strong mid-infrared spectral signature that does not occur in the regions observed by MIDAS. Alternatively, the "p3" pole solution allows a small region of overlap between the PHT-S and SWS fields of view which might contain the source of the ISO mid-infrared spectrum.

7.6.   433 Eros

433 Eros was the only NEA in our survey and was by a wide margin the smallest asteroid we were able to observe. We measured Eros three times, once on 21 September and twice on 22 September. Our sub-Earth points (Giorgini *et al.* 1996) were -83.7° latitude, 92° to 126° longitude on 21 September, and -83.5° latitude, 250° through 320° longitude on 22 September. The subsolar latitude was -88° throughout. The χ^2 fits to our three spectra of 433 Eros are good matches to an STM model with η = 0.72 ± 0.07 and radius R = 10.3 ± 0.5 km. The asteroid's true mean equatorial radius is 9.2 ± 0.1 km (Zuber *et al.* 2000). (Here and in Table 2, we have used the radiometrically derived albedo of Morrison (1976, p = 0.18 ± 0.03) rather than the NEAR narrowband albedos. Albedo estimates for Eros have ranged from 0.125 ± 0.025 (Lebofsky and Rieke 1979, radiometry) to 0.27 ± 0.06 (Veverka *et al.* 2000, NEAR MSI).)

We did not find any evidence for spectral emissivity variation, consistent with up-close near-IR remote sensing and spectroscopy of this asteroid from the NEAR mission (Bell *et al.* 2002). Note that since the subsolar point was so close to the pole, the close match of the asteroid's spectrum to the STM at the time of our observations provides very little constraint on the thermal inertia of Eros.

7.7.   511 Davida

We observed 511 Davida twice on 22 September 2002, calibrating one of our spectra on α Tauri and the other on β Geminorum. The radius we derived, 169 ± 13 km, is consistent with either the IMPS (169 ± 3 km) or SIMPS (163 ± 3 km) results. Our subsolar temperature estimate of 259.5 ± 2.3 K is also entirely consistent with the STM prediction (260.3 K) for the nominal value η = 0.756.

Dotto *et al.* (2002) published a 5.8-11.6 μm ISO PHT-S spectrum of this asteroid. They concluded that its 6.5-11.5 μm behavior resembled that of CM chondrites. Unfortunately, in the region of our spectral coverage, we have been unable to reproduce their results. Within the 3-8% limits of our error bars, our data are uniform in emissivity.

7.8. M-class Asteroids

Recently, several investigators have presented evidence that at least some M-class asteroids cannot be composed of the same material as nickel-iron meteorites. Margot and Brown (2003) discovered a satellite of the M asteroid 22 Kalliope and were able to calculate Kalliope's density at 2.37 ± 0.4 g·cm^{-3}, using the IMPS radius of 90.5 km. They concluded that this is incompatible with a pure nickel-iron composition, since the microporosities of nickel-iron meteorites are very low, and the asteroid's macroporosity would have to exceed that of 253 Mathilde (Yeomans *et al.* 1997) in order to produce the observed density with an iron meteorite composition. Additionally, Rivkin *et al.* (2000) detected 3-μm hydration bands in the spectra of nine out of the 27 M-class asteroids they observed, including 22 Kalliope and 201 Penelope (discussed below) also suggesting that these objects may not be purely metallic in composition.

We measured the mid-infrared spectra of three M-class asteroids during the MIDAS survey. In none of them did we detect any convincing evidence of spectral emissivity variations outside the limits of our uncertainties. We discuss the temperature and radius fitting results below.

7.8.1. 22 Kalliope

We made two sets of nonconsecutive observations of 22 Kalliope on 2 Oct 2001, of 320 seconds/segment each, and one set of observations on 3 Oct 2001. Due to non-photometric conditions, we consider the first set of spectra on 2 October less reliable than the second. On 3 October we enjoyed excellent conditions throughout the night.

Our measured subsolar-point temperatures for 22 Kalliope are 249 ± 3 K, 248 ± 5 K (2 Oct. 2001) and 245 ± 2 K (3 Oct. 2001). The STM prediction for 98% effective emissivity and 14% albedo is 253.2 K. A bolometric albedo of 19% would produce a temperature of 249.6 K, which would be consistent with our temperature results, but would be inconsistent with the IMPS albedo and the radiometrically determined bolometric albedo of 11% of Morrison (1974). Alternatively, Kalliope, which is a fast rotator with a period of 4.148 hours, may have an appreciable thermal inertia. Using the pole solution of Magnusson *et al.* (1993), [α=190°, δ=-6.5°,± 5°, J2000], we find that the sub-Earth and subsolar latitudes at the time of our observations were fairly low (+14° and +36° respectively). If Kalliope's surface temperatures are really being influenced by thermal inertia, the relationship between measured and predicted temperatures should change systematically as a function of subsolar latitude: in the extreme case, where the subsolar point is at a pole, the asteroid should be in thermal equilibrium even for very large values of thermal inertia and the STM prediction would be exact. Additional thermal infrared spectroscopy or multiple-wavelength photometry of this asteroid at different subsolar latitudes should test this hypothesis.

Because our radius estimates were persistently substantially lower than the 90.5 km radius reported by IMPS, we calculated our sub-Earth points using the pole solution and compared our longitudes with the asteroid's well-characterized visible lightcurve. We defined a meridian [W = 10° + 2082.8319108°/day · (Julian Date - 2451545.0)] in

an attempt to have zero longitude coincide with a minimum in the visible lightcurve (Damiani and Foglia 1997; Michalowski and Velichko 1990). Our results are listed as Table 5. We found that both the second observation on October 2 and the observations on October 3 coincided with the longitude of the same minimum of the visible lightcurve. If we accept the axial ratios a/b = 1.32 and b/c = 1.2 and assign our 74 km observed effective radius to $\sqrt{b \cdot c}$, the volume of the asteroid is 90% of the volume of a sphere with the IMPS radius; so this result does not substantially alter the density estimate of Margot and Brown (2003).

The 79 km radius estimate from the first set of spectra on October 2 should be interpreted with caution because these data may have been affected by the non-photometric atmospheric conditions prevalent shortly before they were taken. We report them here because they represent a different aspect from the other measurements of this asteroid.

7.8.2.   201 Penelope

The subsolar temperature measurements for 201 Penelope on 21 September were 255 ± 6 K, with a radius estimate of 37 ± 2 km. The STM predicted a substantially higher temperature (271.8 K) for 98% emissivity and 16% albedo. The temperature measurement for our spectrum from 22 September was also quite low: 250 ± 3 K, with a corresponding radius estimate of 42 ± 2 km. The IMPS radius for this asteroid is 34.2 ± 2 km.

201 Penelope is also a fast rotator, and is more ellipsoidal than 22 Kalliope: Magnusson *et al.* (1993) give the rotation period of Penelope as 0.1561439 days with pole solutions [89°, -27°] or [260°, -27°] in ecliptic coordinates, and axial ratios a/b = 1.5 and b/c = 1.2. The sub-Earth latitude at the time of our observations was either -19° or

+21°. 6.3 rotations of Penelope elapsed between our September 21 and September 22 observations; we could not, therefore, have been observing the same aspect of the asteroid in both cases.

7.8.3. 498 Tokio

The subsolar temperature measurement for 498 Tokio was 301 ± 11 K (3 October 2001). The STM predicted 286.1 K for 7% albedo and 98% emissivity. The best-fit radius for Tokio is 33 ± 2 km, which is significantly lower than the 40.9 ± 1.2 km SIMPS value (Tedesco *et al.* 2002). Because the radius derived from the fit is dependent on the temperature, which in this case due to low signal to noise had high error bars, we recalculated the best-fit radius using a subsolar temperature one standard deviation below that of the chi-squared minimum ($T_{ss} = 289.5$ K). The result was 35.7 $\pm$ 2 km. The asteroid's lightcurve amplitude is ≤ 0.36 magnitudes (Gil-Hutton 1989). Unfortunately a pole solution is not available for 498 Tokio, so we could not determine what relationship our observations have to the asteroid's lightcurve.

7.9. Other Asteroids that Depart from the STM

The mid-infrared spectra of a handful of other asteroids were best fit with a subsolar temperature over one standard deviation away from that predicted by the STM using established albedo values and the standard beaming parameter. These included 18 Melpomene, 24 Themis, 45 Eugenia, 54 Alexandra, and 735 Marghanna. These discrepancies do not appear to be correlated with the phase angles of our observations, as might be expected from phase effects related to infrared beaming. For example, 45 Eugenia was observed at $13.4°$ phase and has a discrepancy of -14 K between the predicted and fitted temperatures; but 3 Juno, observed at $25.3°$ phase, is +8 K above

the STM prediction in temperature, and 109 Felicitas, observed at 25° phase, matches the STM temperature and IMPS radius almost exactly. Similarly, one might expect fast-rotating asteroids observed at low subsolar and sub-Earth latitudes to have lower subsolar-point temperatures (higher η) than the STM would predict. All four of the asteroids for which we derived ($\eta > 0.85$) have rotation periods under nine hours, and the three for which pole solutions are available (Dotto *et al.* 1995; de Angelis 1995; Magnusson *et al.* 1993) were observed at subsolar latitudes $\leq 36°$. However, several other fast rotators (9 Metis, 54 Alexandra, 20 Massalia) observed at low latitudes had normal beaming parameters, and the fifth highest-η asteroid in our survey was the slow rotator 10 Hygiea. These relationships are illustrated in Figs. 12 and 13. This may be evidence for variation in thermal inertia among asteroid surfaces; but one must be cautious since errors in either the bolometric albedo or the infrared phase function can alter the apparent value of η.

Figure 13 shows our derived η values plotted against the phase angles of the MIDAS observations. No high-phase observations (phase angle $\gtrsim 25°$) resulted in spectra that implied high beaming parameters, but the low-phase observations resulted in a wide range of beaming parameter values. Clearly there must be a limiting phase angle beyond which an observer will be out of the sunward "beam" of enhanced thermal emission due to surface roughness; but neither the extent to which that angle varies from asteroid to asteroid nor its location for any given asteroid can be determined from our data alone. Of the two individual asteroids (2 Pallas and 10 Hygiea) that we were able to observe at multiple phase angles, 2 Pallas appeared to have a slightly higher η at 13.5° than at 16° or 18°, but 10 Hygiea produced identical η values for phase angles of 11° and 13.5°. If the thermal infrared spectra of a set of asteroids with well-known spin vectors were observed at multiple phase angles, we would then be able to say more about thermal infrared beaming as a function of phase.

Subsolar-point temperatures below those predicted by the STM may be attributed to the effects of thermal inertia. Higher-than-predicted temperatures, however, such as we find for 18 Melpomene and 54 Alexandra, must be attributed to the other parameters in the temperature prediction: the assumed bolometric albedo or effective emissivity may have been too high or the effects of infrared beaming may have been underestimated ($\eta < 0.756$).

7.9.1. 45 Eugenia

45 Eugenia is unique in our data in the degree of its departure from the standard thermal model. Our best fit is $T_{subsolar} = 232 \pm 4$ K, radius = 79 ± 5 km; whereas the (revised[6]) SIMPS radius is 107.3 ± 2 km, and the STM subsolar temperature prediction is 246.3 K. Thus, both the temperature and size of the asteroid contribute to a large deficit in observed thermal flux compared with the model prediction.

45 Eugenia is a fast rotator (period = 0.2374647 days, Magnusson *et al.* (1993)). Its axial ratio a/b is estimated at 1.36. If we observed Eugenia "end-on", our flux measurement would be consistent with a model in which a/b = 1.36, b = c, and the average radius were equal to the IMPS radius. Using the pole solution of Merline *et al.* (1999), [RA=132°, Dec = -2°, ± 10°], we find that our sub-Earth latitude at the time of our observation was 0.4°± 10°, making an end-on observation plausible.

----

[6]The IMPS (Tedesco 1989) and revised SIMPS (Tedesco *et al.* 2002) radii for 45 Eugenia are 107 ± 4 km and 107.3 ± 2.1 km respectively. The original IMPS albedo was 0.046 ± 0.005; it was revised to 0.0398 ± 0.002.

8. Interpretation

We observe that the great majority of our asteroid spectra have very subdued (< 5 %) spectral contrast in emissivity. Laboratory spectra of minerals (Salisbury *et al.* 1991b; Salisbury 1993) have shown that their mid-infrared features are suppressed at fine particle sizes (Fig. 6a). Moreover, laboratory spectra of powdered meteorite samples (particle size < 75 μm) also display very subtle spectral contrast. In the laboratory spectra of Salisbury *et al.* (1991a), powdered samples have 0.3-1.75% spectral contrast in bidirectional reflectance measurements, which correspond to 1-9% in emission[7]. The mean spectral contrast for the powdered carbonaceous meteorite samples was 3.3%, and the mean for powdered ordinary chondrite samples was 4.7% [8].

We believe that the most straightforward explanation for the lack of substantial emissivity variation in almost all of our asteroid spectra is that these asteroids are covered by fine-grained regoliths. This is consistent with the observation of regolith on 433 Eros by the NEAR MSI investigation (Veverka *et al.* 2001) as well as on Ida and Gaspra by the Galileo SSI team (Belton *et al.* 1992, 1994).

In our best data, we achieved sufficiently high signal to noise ratios to detect subtle (2-3% spectral contrast) features on 4 Vesta that were consistent from night to night. They resemble features observed in laboratory samples of HED meteorites. They do not

---

[7]The laboratory spectra of Salisbury *et al.* [also Calvin and King (1997)] were taken in biconical reflectance and referred to the specular reflectance from an aluminum mirror. For certain samples, Salisbury *et al.* also measured directional-hemispherical reflectance spectra; they found that the biconical and directional-hemispherical spectra closely resembled each other in shape, but that the hemispherical reflectance was about five times higher overall. Since according to Kirchoff's Law the directional-hemispherical reflectance is related to the directional emissivity: $1 - r_{hemispherical} = \epsilon$, the biconical reflectance should be related to the emissivity by $1 - 5 \cdot r_{biconical} = \epsilon$. We have scaled the laboratory data represented in Fig. 9 accordingly.

[8]Barucci *et al.* (2002), however, conducted their own laboratory work on carbonaceous chondritic meteorite samples and concluded that a transparency feature at 11-13 μm was enhanced at small grain sizes.

closely resemble laboratory spectra of chondritic meteorites. We believe that these are likely to be genuinely mineralogical features.

9. Conclusions

Twenty-one of the twenty-nine asteroids in our survey have thermal emission spectra consistent with the predictions of the standard thermal model using an infrared beaming factor η = 0.756 $\pm$ 0.014 and previously established estimates for albedo and radius. Five asteroids had lower than expected temperatures, including two of the three M-class asteroids (22 Kalliope and 201 Penelope). These may reflect low estimates of the bolometric albedo, high estimates of infrared beaming, or the effects of thermal inertia. Their rotation periods range from 3.7 hours (Penelope) to 15.9 hours (735 Marghanna, Mohamed *et al.* (1995)). Three asteroids had higher temperatures than had been predicted by the STM.

With the exception of 1 Ceres, the asteroids in the MIDAS survey have very uniform emissivity throughout our 8.2-13.2 μm wavelength range. Where these results conflict with those of ISO, as they do for 2 Pallas, 4 Vesta, and 10 Hygiea, potential sources of this discrepancy include textural variations, compositional heterogeneity, errors in our flux spectra and/or calibration, or errors in the ISO flux spectra and/or calibration.

Our marginal detection of features on 4 Vesta suggests that future observers may be able to find mineralogical features on these and other main-belt asteroids provided that their spectral uncertainties can be brought below 2%.

Several observers of near-Earth asteroids have suggested that the surface layers of the smallest asteroids may be very different from those of larger objects. For example, Rivkin *et al.* (2003) presented a 1-3.5 μm spectrum of 2002 NY40 that closely resembled an LL6 chondrite spectrum from 1 -3.5 μm, without any of the usual changes attributed

to "space weathering". In addition, Harris *et al.* (1998) published spectrophotometric results for 2100 Ra-Shalom in the thermal infrared. They concluded that it had an unusually high thermal inertia suggestive of an absence of regolith, confirming the earlier results obtained by Lebofsky *et al.* (1979) from radiometry. If the surface layers of these objects contain large exposures of solid rock or areas of particles larger than 75 μm, the laboratory work suggests that their mineralogical spectral emissivity variations should be correspondingly stronger. These kinds of asteroids, when observable, may therefore be more amenable to compositional study in the thermal infrared than their larger counterparts.

10. Acknowledgments

REFERENCES

Barucci, M.A., Dotto, E., Brucato, J.R., Mueller, T.G., Morris, P., Doressoundiram, A., Fulchignoni, M., de Sanctis, M.C., Owen, T., Crovisier, J., Le Bras, A., Colangeli, L., Mennella, V., 2002. "10 Hygiea: ISO Infrared Observations." *Icarus* 156, 202-210.

Bell III, J.F., Izenberg, N.I., Lucey, P.G., Clark, B.E., Peterson, C., Gaffey, M.J., Joseph, J., Carcich, B., Harch, A., Bell, M.E., Warren, J., Martin, P.D., McFadden, L.A., Wellnitz, D., Murchie, S., Winter, M., Veverka, J., Thomas, P., Robinson, M.S., Malin, M., Cheng, A., 2002. "Near-IR Reflectance Spectroscopy of 433 Eros from the NIS Instrument on the NEAR Mission. 1. Low Phase Angle Observations." *Icarus* 155, 119-144.

Belton, M.J.S., Veverka, J., Thomas, P., Helfenstein, P., Simonelli, D., Chapman, C., Davies, M.E., Greeley, R., Greenberg, R., Head, J., Murchie, S., Klaasen, K., Johnson, T.V., McEwen, A., Morrison, D., Neukum, G., Fanale, F., Anger, C., Carr, M., Pilcher, V., 1992. "Galileo Encounter with 951 Gaspra: First Pictures of an Asteroid." *Science* 257, 1647-1652.

Belton, M.J.S., Chapman, C.R., Veverka, J., Klaasen, K.P., Harch, A., Greeley, R., Greenberg, R., Head III, J.W., McEwen, A., Morrison, D., Thomas, P.C., Davies, M.E., Carr, M.H., Neukum, G., Fanale, F.P., Davis, D.R., Anger, C., Gierasch, P.J., Ingersoll, A.P., Pilcher, V., 1994. "First Images of Asteroid 243 Ida." *Science* 265, 1543-1547.

Bevington, P.R., and Robinson, D.K., York, 1992. *Data Reduction and Error Analysis for the Physical Sciences, 2nd ed.* McGraw-Hill, New York.

Bus, S.J., 1999. *Compositional Structure in the Asteroid Belt: Results of a Spectroscopic Survey.* Ph.D. Thesis, Massachusetts Institute of Technology, Cambridge, MA.

Calvin, W.M., and King, T.V.V. 1997. "Spectral characteristics of iron-bearing phyllosilicates: Comparison to Orgueil (CI1), Murchison and Murray (CM2)." *Meteoritics & Planetary Science* 32, 693-701.

Cohen, M., Walker, R.G., Witteborn, F.C. 1992. "Spectral irradiance calibration in the infrared. II - α Tau and the recalibration of the IRAS low resolution spectrometer." *AJ* 104, 2030-2044. [Paper II]

Cohen, M., Witteborn, F.C., Roush, T., Bregman, J.D., Wooden, D.H., 1998. "Spectral Irradiance Calibration in the Infrared. VIII. 5-14 Micron Spectroscopy of the Asteroids Ceres, Vesta, and Pallas." *AJ* 115, 1671. [Paper VIII]

Cohen, M., Walker, R.G., Carter, B., Hammersley, P., Kidger, M., Noguchi, K., 1999. "Spectral Irradiance Calibration in the Infrared. X. A Self-Consistent Radiometric All-Sky Network of Absolutely Calibrated Stellar Spectra." *AJ* 117, 1864-1889. [Paper X]

Damiani, M., Foglia, S., 1997. "Photoelectric photometry of 22 Kalliope." *Minor Planet Bulletin* 24, 13.

De Angelis, G. 1995. "Asteroid spin, pole, and shape determinations." *Planet. Space Sci.* 43, 649-682.

Dotto, E., Barucci, M. A., Mueller, T. G., Brucato, J. R., Fulchignoni, M., Mennella, V., Colangeli, L., 2002. "ISO observations of low and moderate albedo asteroids: PHT-P and PHT-S results." *A&A* 393, 1065-1072.

Dotto, E., de Angelis, G., di Martino, M., Barucci, M.A., Fulchignoni, M., de Sanctis, G., Burchi, R., 1995. "Pole orientation and shape of 12 asteroids." *Icarus* 117, 313-327.

Dotto, E., Mueller, T.G., Barucci, M.A., Encrenaz, Th, Knacke, R.F., Lellouch, E., Doressoundiram, A., Crovisier, J., Brucato, J.R., Colangeli, L., Mennella, V.,

2000. "ISO results on bright Main Belt asteroids: PHT-S observations." *A&A* 358, 1133-1141.

Drummond, J.D., Fugate, R.Q., Christou, J.C., Hege, E.K.,1998. "Full Adaptive Optics Images of Asteroids Ceres and Vesta; Rotational Poles and Triaxial Ellipsoid Dimensions." *Icarus* 132, 80-99.

Dunham, D.W., Dunham, J.B., Binzel, R.P., Evans, D.S., Freuh, M., Henry, G.W., A'Hearn, M.F., Schnurr, R.G., Betts, R., Haynes, H., Orcutt, R., Bowell, E., Wasserman, L.H., Nye, R.A., Giclas, H.L., Chapman, C.R., Dietz, R.D., Moncivais, C., Douglass, W.T., Parker, D.C., Beish, J.D., Martin, J.O., Monger, D.R., Hubbard, W.B., Reitsema, H.J., Klemola, A.R., Lee, P.D., McNamara, B.R., Maley, P.D., Manly, P., Markworth, N.L., Nolthenius, R., Oswalt, T.D., Smith, J.A., Strother, E.F., Povenmire, H.R., Purrington, R.D., Trenary, C., Schneider, G.H., Schuster, W.J., Moreno, M.A., Guichard, J., Sanchez, G.R., Taylor, G.E., Upgren, A.R., von Flandern, T.C., 1990. "The size and shape of (2) Pallas from the 1983 occultation of 1 Vulpeculae." *AJ* 99, 1636-1662.

Erikson, A., Magnusson, P., 1993. "Pole Determinations of Asteroids." *Icarus* 103, 62-66.

Feierberg, M.A., Witteborn, F.C, Lebofsky, L.A.,1983. "Detection of Silicate Emission Features in the 8-to 13-micron Spectra of Main Belt Asteroids." *Icarus* 56, 393-397.

Gil-Hutton, R., 1989. "V+B Photoelectric Photometry of Asteroids 45 Eugenia and 498 Tokio." *Minor Planet Bulletin* 16, 16-17

Gillett, F.C., Merrill, K.M., 1975. "7.5-13.5 micron spectra of Ceres and Vesta." *Icarus* 26, 358-360.

Giorgini, J.D., Yeomans, D.K., Chamberlin, A.B., Chodas, P.W., Jacobson, R.A., Keesey, M.S., Lieske, J.H., Ostro, S.J., Standish, E.M., Wimberly, R.N., 1996. "JPL's On-Line Solar System Data Service." *BAAS* 28 (3), 1158.

Green, S. F., Eaton, N., Aitken, D. K., Roche, P. F., Meadows, A. J., 1985. "8- to 13-micron Spectra of Asteroids." *Icarus* 62, 282-288.

Hayward, T.L., Miles, J.W., Houck, J.R., Gull, G.E., Schoenwald, J., 1993. "SpectroCam-10: A 10-micron spectrograph/camera for the Hale Telescope" *Proc. SPIE* 1946, 334.

Harris, A.W., 1996. "Asteroid Lightcurve Derived Data V2.0" *Planetary Data System - Small Bodies Node (PDSSBN)*, (M. A'Hearn, University of Maryland, College Park, Maryland) http://pdssbn.astro.umd.edu

Harris, A. W., 1998. "A Thermal Model for Near-Earth Asteroids." *Icarus* 131, 291-301.

Harris, A. W., Davies, J.K., Green,S.F., 1998. "Thermal Infrared Spectrophotometry of the Near-Earth Asteroids 2100 Ra-Shalom and 1991 EE." *Icarus* 135, 441-450.

King, T.V.V., Clark, R.N., Calvin, W.M., Sherman, D.M., Brown, R.H., 1992. "Evidence for ammonium-bearing minerals on Ceres." *Science* 255, 1551-1553.

Kristensen, L. K., 1984. "(9) Metis okkultationen den 19 februar 1984." *Astronomi & Rumfart* Maj-Jun 1984, 76-78.

Lebofsky, L. A., Lebofsky, M.J., Rieke, G.H., 1979. "Radiometry and surface properties of Apollo, Amor, and Aten asteroids." *AJ* 84, 885-888.

Lebofsky, L. A., Rieke, G. H., 1979. "Thermal Properties of 433 Eros." *Icarus* 40, 297-308.

Lebofsky, L. A., Spencer, J., 1989. "Radiometry and Thermal Modeling of Asteroids" In: Binzel, R.P., Gehrels, T., Matthews, M.S. (Eds.), *Asteroids II*. Univ. of Arizona Press, Tucson, pp. 128-147.

Lebofsky, L. A., Sykes, M.V., Tedesco, E.F., Veeder, G.J., Matson, D.L., Brown, R.H., Gradie, J.C., Feierberg, M.A., Rudy, R.J., 1986. "A refined 'standard' thermal model for asteroids based on observations of 1 Ceres and 2 Pallas." *Icarus* 68, p. 239-251.

Logan, L. M., Hunt, G.R., Salisbury, J.W., Balsamo, S.R., 1973. "Compositional implications of Christiansen frequency maximums for infrared remote sensing applications." *J. Geophys. Res.* 78, 4983-5003.

Lopez-Gonzalez, M. J., Rodriguez, E., 2000. "Lightcurves of 10 Hygiea, 241 Germania and 509 Iolanda." *Astron. Astrophys. Suppl. Ser.* 145, 255-261.

Lord, S. D., 1992. "A new software tool for computing Earth's atmospheric transmission of near- and far-infrared radiation." NASA Technical Memor. 103957.

Magnusson, P., Lagerkvist, C.-I., Dahlgren, M., Erikson, A., Barucci, M.A., Belskaya, I., Capria, M.T., 1993. "The Uppsala Asteroid Data Base", In: Milani, A., Di Martino, M., Cellini, A. (Eds.), *Asteroids, Comets, Meteors.* Kluwer Academic Publishers, Dordrecht, pp. 471-476.

Margot, J.-L, Brown, M.E., 2003. "A Low-Density M-type Asteroid in the Main Belt." *Science* 300, 1939-1942.

Matson, D.L., 1971b. *I. Astronomical Photometry at Wavelengths of 8.5, 10.5, , 8.5, and 11.6 micrometers. II. Infrared Emission from Asteroids at Wavelengths of 8.5, 10.5, and 11.6 micrometers.* Ph. D. Thesis, California Institute of Technology.

Matson, D.L., ed. 1986. *IRAS Asteroid and Comet Survey* (JPL Doc. D-3698) (Pasadena: JPL)

Merline, W.J., Close, L.M., Dumas, C., Chapman, C.R., Roddier, F., Menard, F., Slater, D.C., Duvert, G., Shelton, C., Morgan, T., 1999. "Discovery of a moon orbiting the asteroid 45 Eugenia." *Nature* 401, 565-568.

Michalowski, T., Velichko, F.P., 1990. "Photoelectric photometry, parameters of rotation and shapes of asteroids 22 Kalliope and 79 Eurynome." *Acta Astron.* 40, 321-332.

Michalowski, T., Velichko, F.P., Lindgren, M., Oja, T., Lagerkvist, C.-I., Magnusson, P., 1991. "The spin vector of asteroid 10 Hygiea." *Astron. Astrophys. Suppl. Ser.* 91, 53-59.

Millis, R. L, Wasserman, L.H., Bowell, E., Franz, O.G., White, N.M., Lockwood, G.W., Nye, R., Bertram, R., Klemola, A., Dunham, E., Morrison, D., 1981. "The diameter of Juno from its occultation of AG+0°1022." *AJ* 86, 306-313.

Millis, R. L., and 41 colleagues 1987. The size, shape, density, and albedo of Ceres from its occultation of BD+8 deg 471. *Icarus* 72, 507-518.

Mohamed, R. A., Krugly, Y.N., Yurij, N., Lupishko, D.R., 1995. "Light curves and rotation periods of asteroids 371 Bohemia, 426 Hippo, 480 Hansa, and 735 Marghanna." *AJ* 109, 1877-1879.

Morrison, D., 1974. "Radiometric Diameters and Albedos of 40 Asteroids." *AJ* 194, 203-212.

Morrison, D., 1976. "The Diameter and Thermal Inertia of 433 Eros." *Icarus* 28, 125-132.

Mueller, T. G., Blommaert, J. A. D. L. 2004. "65 Cybele in the thermal infrared: Multiple observations and thermophysical analysis." *A&A* 418, 347-356.

Parker, J. W., Stern, S.A., Thomas, P.C., Festou, M.C., Merline, W.J., Young, E.F., Binzel, R.P., Lebofsky, L.A., 2002. "Analysis of the First Disk-Resolved Images of Ceres from Ultraviolet Observations with the Hubble Space Telescope." *AJ* 123, 549-557.

Rivkin, A. S., Howell, E.S., Lebofsky, L.A., Clark, B.E., Britt, D.T., 2000. "The Nature of M-Class Asteroids from 3-micron Observations." *Icarus* 145, 351-368.

Rivkin, A. S., Howell, E.S., Bus, S.J., Hicks, M., Reach, W.T., Jarrett, T.H., Binzel, R.P., 2003. "Spectroscopy and Photometry of the Earth Grazer 2002 NY40." Abstract 1722 from the 34th Annual Lunar and Planetary Science Conference, League City, Texas, March 17-21, 2003.

Salisbury, J. W., D'Aria, D.M., Jarosewich, E., 1991. "Midinfrared (2.5-13.5 μm) reflectance spectra of powdered stony meteorites." *Icarus* 92, 280-297.

Salisbury, J. W., Walter, L.S., Vergo, N., D'Aria, D.M., 1991. *Infrared (2.1- 25 micrometers) Spectra of Minerals.* Johns Hopkins University Press.

Salisbury, J. W. 1993. "Mid-Infrared Spectroscopy: Laboratory Data." In: Pieters, C.M., Englert, P.A.J. (Eds.), *Remote Geochemical Analysis: Elemental and Mineralogical Composition.* Cambridge University Press, pp. 79-98.

Spencer, J. R., Lebofsky, L.A., Sykes, M.V., 1989. "Systematic Biases in Radiometric Diameter Determinations." *Icarus* 78, 337-354.

Tedesco, E. F., 1989. "Asteroid Magnitudes, UBV Colors, and IRAS Albedos and Diameters." In: Binzel, R.P., Gehrels, T., Matthews, M.S. (Eds.), *Asteroids II.* Univ. of Arizona Press, Tucson, pp. 1090-1138.

Tedesco, E. F., Noah, P.V., Noah, M., Price, S.D., 2002. "The Supplemental *IRAS* Minor Planet Survey." *AJ* 123: 1056-1085.

Tholen, D. J., 1989. "Asteroid Taxonomic Classifications." In: Binzel, R.P., Gehrels, T., Matthews, M.S. (Eds.), *Asteroids II.* Univ. of Arizona Press, Tucson, pp. 1139-1150.

Tholen, D. J. 2000. EPHEM v. 1.2 (Asteroid ephemeris software, updated with MPC data every three months.)

Thomas, P. C., Binzel, R.P., Gaffey, M.J., Storrs, A.W., Wells, E., Zellner, B., 1997. "Vesta: Spin pole, size, and shape from HST images." *Icarus* 128, 88-94.

Veverka, J., and 32 colleagues 2000. NEAR at Eros: Imaging and Spectral Results. Science 289, 2088-2097.

Veverka, J., Thomas, P.C., Robinson, M., Murchie, S., Chapman, C., Bell, M., Harch, A., Merline, W.J., Bell III, J.F., Bussey, B., Carcich, B., Cheng, A., Clark, B., Domingue, D., Dunham, D., Farquhar, R., Gaffey, M.J., Hawkins, E., Izenberg, N., Joseph, J., Kirk, R., Li, H., Lucey, P., Malin, M., McFadden, L., Miller, J.K., Owen, W.M., Peterson, C., Prockter, L., Warren, J., Wellnitz, D., Williams, B.G., Yeomans,D.K., 2001. "Imaging of Small-Scale Features on 433 Eros from NEAR: Evidence for a Complex Regolith." *Science* 292, pp. 484-488.

Witteborn, F. C., Cohen, M., Bregman, J.D., Wooden, D.H., Heere, K., Shirley, E.L.,1999. "Spectral Irradiance Calibration in the Infrared. XI. Comparison of α Bootis and 1 Ceres with a Laboratory Standard." *AJ* 117, 2552-2560.

Yeomans, D. K., Barriot, J.-P., Dunham, D.W., Farquhar, R.W., Giorgini, J.D., Helfrich, C.E., Konopliv, A.S., McAdams, J.V., Miller, J.K., Jr., W.M.Owen, Scheeres, D.J., Synnott, S.P., Williams, B.G., 1997. "Estimating the Mass of Asteroid 253 Mathilde from Tracking Data During the NEAR Flyby." *Science* 278, 2106.

Zuber, M. T., Smith, D.E., Cheng, A.F., Garvin, J.B., Aharonson, O., Cole, T.D., Dunn, P.J., Guo, Y., Lemoine, F.G., Neumann, G.A., Rowlands, D.D., Torrence, M.H., 2000. "The Shape of 433 Eros from the NEAR-Shoemaker Laser Rangefinder." *Science* 289, 2097-2101.

This manuscript was prepared with the AAS LATEX macros v5.2.

Figure and Table Captions

Table 1:   Circumstances of asteroid observations.

Table 2:   STM temperature and radius fitting results.

"Published radius" values are from the Supplemental IRAS Minor Planet Survey (Tedesco *et al.* 2002) except where noted. The "assumed albedo" is the albedo used to calculate the "STM Predicted $T_{subsolar}$." These albedos have been taken from Tedesco *et al.* (2002) except as follows: 3 Juno and 4 Vesta, Morrison (1974); 9 Metis and 24 Themis, Giorgini *et al.* (1996); 433 Eros, Morrison (1976). "Rotation Period": Giorgini *et al.* (1996); Harris (1996).

Table 3:   Sub-Earth and sub-solar points of 4 Vesta at the times of ISO and MIDAS observations.

Table 4:   Sub-Earth and sub-solar points of 10 Hygiea at the times of ISO and MIDAS observations.

Table 5:   Sub-Earth and sub-solar points of 22 Kalliope at the times of MIDAS observations.

Figure 1:   Calibration stars.

Ratio of the spectrum of α Tauri published by Cohen *et al.* (1992) to the blackbody spectrum used as a reference for this star by Gillett and Merrill (1975).

Figure 2:   SC-10 data processing.

2a. Background substraction via on-chip chopping and nodding.

2b. Spatial profile. This is the sum across all wavelengths of the SC-10 detector signal from one segment. The central peak represents the two overlapping positive images (see Fig. 2a). The flanking images represent the opposite chop positions.

2c. Raw data from the same SC-10 segment as a two-dimensional image. The spectral dispersion is left-right, with wavelength increasing toward the left. The vertical direction is spatial.

Figure 3: Spectra of γ Aquilae ratioed to a 4000 K blackbody.

Top: γ Aql as measured in the current work. This spectrum is an average of three spectra calibrated on α Lyrae and β Pegasi.

Bottom: Template spectrum published for γ Aql by Cohen *et al.* (1999) The template is based on α Hydrae shortward of 10.3 μm and on a theoretical model longward of 10.6 μm.

Figure 4: Model atmospheric transmission for Palomar (ATRAN, Lord (1992)). Atmospheric transmission as a function of wavelength in the mid-infrared. The large absorption between 9.2 and 10.1 μm is caused by telluric ozone; most of the other structure is due to water vapor. The transmission function has been smoothed to the spectral resolution of SC-10's low-resolution mode.

Figure 5: Wavelength registration of SC-10 data.

Upper plot: Non-flux-calibrated spectral data from an asteroid (dot-dashed line) and a standard star (solid line). The shaded areas mark strong telluric features. Lower plot: Ratios of asteroid to standard spectra. The solid line here is the ratio of the correctly wavelength-calibrated raw spectra; the dotted line is the ratio when the source and standard spectra are misregistered in wavelength with respect to each other. Incorrect wavelength registration of the raw spectra causes substantial artifacts in the ratio at wavelengths where there is a slope in the atmospheric transmission function.

Figure 6: Mid-infrared spectra of laboratory materials.

6a. The effect of particle size on the strength of mid-infrared spectral features. At small grain sizes the features are suppressed but do not change in wavelength.

Data from Salisbury *et al.* (1991b).

6b. Laboratory spectra of powdered meteorite samples.

Data from Salisbury *et al.* (1991a). The right-hand axis is the emissivity derived from bidirectional reflectance data (see footnote in "Interpretation") for easier comparison with the current work. The Allende and Johnstown spectra have been offset in reflectance by 1.5% and 3% respectively from La Criolla for clarity.

Figure 7:   Mid-infrared flux spectra of the twenty-nine "MIDAS" asteroids.

The data have been binned to 0.1 μm resolution. The error bars represent the standard deviation of the points in each bin. The dashed lines represent the best-fit STM for each spectrum. The shaded grey areas are regions of strong telluric absorptions. Data points within those wavelength regions should be regarded as suspect.

Figure 8:   Emissivity spectra of selected asteroids.

These were produced by dividing the flux spectra in Fig. 7 by the best-fit STM thermal models. Again, the grey shaded areas represent wavelength regions where the data are prone to systematic errors due to strong telluric absorption features.

Figure 9:   Thermal Infrared Spectra of 4 Vesta and various laboratory materials.

Laboratory data from Salisbury *et al.* (1991a) and Salisbury *et al.* (1991b) For the relationship between biconical reflectance and emissivity, see footnote in "Interpretation".

Figure 10:   MIDAS and ISO sub-Earth points and fields of view for 4 Vesta.

Shaded areas are within 70° of the sub-Earth point. The pole solution used was [301°, 41°] (Thomas *et al.* 1997). See Table 3 for the times and coordinates of each measurement.

Figure 11:   MIDAS and ISO sub-Earth points and fields of view for 10 Hygiea.

Again, points within 70° of the sub-Earth point are considered to be inside the field of view. See Table 4 for the times and coordinates of each measurement.

11a. Sub-Earth points calculated using the "p3" pole solution, [120°, 34°]. The ISO SWS observation lasted for over three hours, so we have represented both its starting and ending sub-Earth points on the map joined by a line.

11b. Sub-Earth points calculated using the "p4" pole solution, [295°, 43°].

Figure 12:   Rotation rates and MIDAS radii.

Asteroid measurements with unusually high ($\eta > 0.85$) beaming parameters are marked with diamonds.

Figure 13:   Derived beaming parameters (η) vs. phase angles of MIDAS observation.

Table 1: Circumstances of Asteroid Observations

Asteroid	Total integration time per segment (s)	Observation Date (UT)	Start Time (UT)	End Time (UT)	Integration time per segment (s)	Standard Stars	
1 Ceres	477	2002-Sep-21	7:52:19	8:31:55	318	η Cet	
		2002-Sep-22	8:07:02	8:18:47	159	α Cet	
2 Pallas	956	2001-Oct-03	3:02:58	3:23:00	320	γ Aql	β And
		2002-Sep-22	3:25:52	3:57:35	318	γ Aql	
		2003-Aug-22	11:47:02	11:56:19	159	α Cet	
		2003-Aug-23	12:00:07	12:17:04	159	α Cet	
3 Juno	160	2001-Oct-02	13:23:11	13:32:28	160	β Gem	
4 Vesta	960	2001-Oct-02	09:59:28	10:19:40	320	α Tau	
		2001-Oct-02	10:40:07	10:59:37	320[†]	α Tau	
		2001-Oct-03	11:00:30	11:44:55	320	α Tau	
9 Metis	160	2001-Oct-02	13:41:53	13:51:12	160	β Gem	
10 Hygiea	798	2001-Oct-03	5:03:33	5:28:25	320	α Lyr	
		2002-Sep-21	10:02:05	10:30:59	318	α Tau	
		2002-Sep-22	13:46:38	14:00:49	159	α Tau	
11 Parthenope	320	2001-Oct-02	11:47:19	12:07:23	320	α Tau	
15 Eunomia	159	2002-Sep-22	4:32:39	4:48:08	159	γ Aql	β Peg
18 Melpomene	159	2002-Sep-22	7:45:06	7:58:00	159	η Cet	
20 Massalia	318	2002-Sep-21	12:35:01	13:01:50	318	α Tau	
22 Kalliope	641	2001-Oct-02	11:08:28	11:27:58	320[‡]	α Tau	
		2001-Oct-02	12:29:38	13:01:07	320	α Tau	β Gem
		2001-Oct-03	13:30:44	14:03:15	320	α Tau	
24 Themis	320	2002-Oct-03	12:48:21	13:11:31	320	α Tau	
25 Phocaea	318	2002-Sep-22	2:26:19	2:48:08	318	γ Aql	α Lyr
40 Harmonia	320	2001-Oct-03	11:52:43	12:29:23	320	α Tau	
45 Eugenia	318	2002-Sep-22	9:59:25	10:25:00	318	α Cet	
46 Hestia	159	2002-Sep-21	10:55:47	11:08:28	159	α Tau	
54 Alexandra	320	2001-Oct-03	3:57:43	4:17:58	320	α Lyr	
89 Julia	160	2001-Oct-03	9:54:29	10:03:47	160	α Tau	
95 Arethusa	320	2001-Oct-03	5:55:40	7:15:18	320	β Peg	
109 Felicitas	318	2002-Sep-21	13:38:01	14:14:40	318	α Tau	
137 Meliboea	159	2002-Sep-22	9:20:07	9:34:38	159	α Cet	
200 Dynamene	318	2002-Sep-22	11:37:30	12:08:59	318	α Cet	
201 Penelope	477	2002-Sep-21	9:01:27	9:33:23	318	α Cet	
		2002-Sep-22	8:41:57	8:54:25	159	α Cet	β And
240 Vanadis	318	2002-Sep-21	11:35:19	12:07:00	318	α Tau	
433 Eros	955	2002-Sep-21	5:47:55	6:23:00	318	β Peg	β And
		2002-Sep-22	5:16:29	5:46:06	318	β Peg	β And
		2002-Sep-22	6:16:23	6:46:28	318	β And	
498 Tokio	160	2002-Oct-03	8:39:43	8:49:00	160	α Tau	
511 Davida	318	2002-Sep-22	12:41:15	13:13:59	318	α Tau	β Gem
704 Interamnia	320	2001-Oct-03	7:31:13	8:31:09	318	β And	
735 Marghanna	318	2002-Sep-22	10:46:26	11:12:46	318	α Cet	

[†] Slit losses due to tracking problems. This observation has been included in the emissivity average in Fig. 8 but not in the flux average of Fig. 7.
[‡] Marginal conditions. This observation has been included in Table 2 but not in the average spectra in Figs. 7 and 8.

Table 2: STM Temperature and Radius Fitting Results

Asteroid	Fitted $T_{subsolar}$ (K)	Fitted Radius (km)	Implied Beaming Param. (η)	STM Pred. $T_{subsolar}$ ($\eta = 0.756$) (K)	Published Radius (km)	Assumed Albedo	Assumed Emissivity	Phase Angle (degrees)	Taxonomic Class (Bus 1999)	Taxonomic Class (Tholen 1989)	Rotation Period (hours)
1 Ceres (21 Sept. 2002)	241.6 ± 1.4	470.5 ± 25.0	0.74 ± 0.02	240.5	475.5 ± 3.9[a]	0.11	0.98	7.47°	C	G	9.07
1 Ceres (22 Sept. 2002)	241.8 ± 1	467.7 ± 25.0	0.74 ± 0.01	240.6	475.5 ± 3.9[a]	0.11	0.98	6.93°	C	G	9.07
2 Pallas (3 Oct. 2001)	230.9 ± 1.6	279.1 ± 18.0	0.71 ± 0.02	227.6	266 ± 3[b]	0.16	0.95	16.42°	B	B	7.813
2 Pallas (22 Sept. 2002)	221.6 ± 1.3	276.0 ± 17.0	0.78 ± 0.02	223.5	266 ± 3[b]	0.16	0.95	13.51°	B	B	7.813
2 Pallas (22-23 Aug. 2003)	245 ± 3	291.7 ± 15.0	0.74 ± 0.04	243.3	266 ± 3[b]	0.16	0.95	17.93°	B	B	7.813
3 Juno	292.8 ± 7	135.7 ± 11.0	0.67 ± 0.07	284.6	134 ± 3[c]	0.15	0.95	25.27°	Sk	S	7.21
4 Vesta (2 Oct. 2001)	250.5 ± 1.3	262.7 ± 19.0	0.75 ± 0.01	250.2	265 ± 5[d]	0.24	0.95	20.66°	V	V	5.342
4 Vesta (3 Oct. 2001)	246.8 ± 1	256.4 ± 18.0	0.80 ± 0.01	250.2	265 ± 5[d]	0.24	0.95	20.47°	V	V	5.342
9 Metis	282.2 ± 12.1	78.2 ± 7.0	0.75 ± 0.14	281.7	95 ± 10[e]	0.18	0.95	28.32°		S	5.079
10 Hygiea (3 Oct. 2001)	229.7 ± 3.2	224.0 ± 13.0	0.80 ± 0.05	233.3	204 ± 3[f]	0.07	0.98	10.8°	C	C	27.623
10 Hygiea (21 Sept. 2002)	219.7 ± 3.7	209.7 ± 13.0	0.81 ± 0.06	223.6	204 ± 3[f]	0.07	0.98	13.46°	C	C	27.623
10 Hygiea (22 Sept. 2002)	218.8 ± 2.6	213.8 ± 13.0	0.82 ± 0.04	223.6	204 ± 3[f]	0.07	0.98	13.24°	C	C	27.623
11 Parthenope	264.2 ± 3.4	65.5 ± 5.0	0.74 ± 0.04	262.7	76.67 ± 2	0.18	0.95	20.31°	Sk	S	
15 Eunomia	269.1 ± 9	145.7 ± 8.0	0.78 ± 0.11	271.1	127.67 ± 8[g]	0.21	0.95	9.17°	S	S	6.083
18 Melpomene	310.1 ± 4.1	74.6 ± 4.0	0.65 ± 0.04	299.2	70.29 ± 1	0.22	0.95	7.57°	S	S	11.57
20 Massalia	270.5 ± 2.6	77.2 ± 7.0	0.80 ± 0.03	274.5	72.75 ± 5	0.21	0.95	27.15°	S	S	8.098
22 Kalliope (2 Oct. 2001)	248.8 ± 3.4	78.9 ± 6.0	0.81 ± 0.05	253.2	90.5 ± 2	0.14	0.98	22.01°	X	M	4.148
22 Kalliope (2 Oct. 2001)	247.7 ± 5	73.0 ± 5.0	0.82 ± 0.07	253.2	90.5 ± 2	0.14	0.98	22°	X	M	4.148
22 Kalliope (3 Oct. 2001)	244.5 ± 2.9	74.3 ± 6.0	0.87 ± 0.04	253.2	90.5 ± 2	0.14	0.98	21.92°	X	M	4.148
24 Themis	230.6 ± 4.2	104.9 ± 7.0	0.90 ± 0.07	240.8		0.07	0.98	18.34°	B	C	8.37
25 Phocaea	303.8 ± 6	41.0 ± 4.0	0.72 ± 0.06	299.9	37.56 ± 2	0.23	0.95	33.59°	S	S	9.9
40 Harmonia	270.7 ± 4.6	54.5 ± 5.0	0.73 ± 0.05	268.8	53.81 ± 3	0.24	0.95	26.5°	S	S	8.9
45 Eugenia	231.8 ± 4.2	78.7 ± 5.0	0.96 ± 0.07	246.3	107.32 ± 2	0.04	0.98	13.42°	C	FC	5.699
46 Hestia	287.8 ± 6.8	62.9 ± 5.0	0.75 ± 0.07	286.8	62.07 ± 2	0.05	0.98	22.17°	Xc	P	21.7
54 Alexandra	283.1 ± 3.5	68.6 ± 4.0	0.65 ± 0.03	272.4	82.88 ± 2	0.06	0.98	10.17°	C	C	7.026
89 Julia	279.6 ± 5.9	73.3 ± 5.0	0.74 ± 0.06	278	75.73 ± 2	0.18	0.95	20.35°	K	S	11.38
95 Arethusa	256.4 ± 2.1	64.5 ± 3.2	0.74 ± 0.02	255.3	68.02 ± 5	0.07	0.98	6.6°	Ch	C	8.68
109 Felicitas	296.9 ± 4.4	43.2 ± 3.0	0.77 ± 0.05	297.9	44.72 ± 1	0.07	0.98	24.95°	Ch	GC	13.2
137 Meliboea	263.3 ± 3.7	73.1 ± 3.7	0.72 ± 0.04	259.8	72.71 ± 2	0.05	0.98	3.7°		C	15
200 Dynamene	271 ± 4.6	61.7 ± 4.0	0.76 ± 0.05	271.4	64.18 ± 1	0.05	0.98	20.71°	Ch	C	19
201 Penelope (21 Sept. 2002)	254.8 ± 6.2	36.6 ± 1.8	0.98 ± 0.10	271.8	34.19 ± 2	0.16	0.98	8.85°	X	M	3.747
201 Penelope (22 Sept. 2002)	249.9 ± 2.5	41.8 ± 2.1	1.06 ± 0.04	271.8	34.19 ± 2	0.16	0.98	8.38°	X	M	3.747
240 Vanadis	292.9 ± 5.1	52.2 ± 2.6	0.71 ± 0.05	288.6	51.95 ± 1	0.04	0.98	27.05°	C	C	
433 Eros (21 Sept. 2002)	326.8 ± 9.1	10.2 ± 0.5	0.71 ± 0.08	321.5	9.2 ± 0.1[h]	0.18	0.95	14.5°	S	S	5.27
433 Eros (22 Sept. 2002)	325 ± 7	10.6 ± 0.5	0.73 ± 0.07	321.8	9.2 ± 0.1[h]	0.18	0.95	14.95°	S	S	5.27
433 Eros (22 Sept. 2002)	327.8 ± 7.8	10.2 ± 0.5	0.70 ± 0.07	321.8	9.2 ± 0.1[h]	0.18	0.95	14.97°	S	S	5.27
498 Tokio	300.8 ± 11.3	32.6 ± 1.6	0.62 ± 0.10	286.1	40.9 ± 1.1	0.07	0.98	8.74°		M	
511 Davida	259.5 ± 2.3	168.6 ± 13.0	0.76 ± 0.03	260.3	163.03 ± 2.7[i]	0.05	0.98	22.46°	C	C	5.129
704 Interamnia	254 ± 1.6	173.9 ± 10.0	0.80 ± 0.02	257.9	158.31 ± 3[j]	0.07	0.98	10.61°	B	F	8.69
735 Marghanna	298.2 ± 3.9	36.6 ± 3.0	0.82 ± 0.04	304.2	37.16 ± 1	0.05	0.98	22.82°	Ch	C	

[a] Parker et al. (2002), HST imaging. SIMPS (Tedesco et al., 2002): R = 424 ± 10 km. See Footnote 2 on SIMPS radii for very large asteroids.

[b] Dunham et al. (1990), occultation. SIMPS (Tedesco et al., 2002): R = 249 ± 9 km.

[c] Millis et al. (1981), occultation. SIMPS (Tedesco et al., 2002): R = 117 ± 6 km.

[d] Thomas et al. (1997), HST imaging (mean radius) SIMPS (Tedesco et al., 2002): R = 234 ± 13 km.

[e] Kristensen (1984), occultation. No IRAS diameter.

[f] Original (Tedesco 1989) IMPS radius was R = 215 ± 4 km.

[g] Original (Tedesco 1989) IMPS radius was R = 136 ± 3 km.

[h] Zuber et al. (2000), NLR laser ranging (mean equatorial radius). We cite the equatorial radius here because our sub-Earth point was within 3° of the asteroid's south pole.
The mean overall radius of Eros is 7.31 ± 0.01 km.

[i] Original IMPS radius was R = 169 ± 3 km.

[j] Original IMPS radius was R = 167 ± 3 km.

Table 3: 4 Vesta Sub-Earth and Sub-Solar Points

Observation	Date	Time(UT)	Subsolar Point		Sub-Earth Point	
			Lat.	W. Long.	Lat.	W. Long.
ISO (PHT-S)	1996-Dec-06	17:59:33	-19°	221°	-11°	198°
MIDAS	2001-Oct-02	10:40	7°	73°	18°	56°
MIDAS	2001-Oct-02	11:00	7°	96°	18°	78°
MIDAS	2001-Oct-03	11:00	7°	273°	18°	256°
MIDAS	2001-Oct-03	11:40	7°	317°	18°	300°

Table 4: 10 Hygiea Sub-Earth and Sub-Solar Points

			"p3" Pole Solution: $\alpha=120°$, $\delta=34°$				"p4" Pole Solution: $\alpha=295°$, $\delta=43°$			
Observation	Date	Time(UT)	Subsolar Point		Sub-Earth Point		Subsolar Point		Sub-Earth Point	
			Lat.	W. Long.	Lat.	W. Long.	Lat.	W. Long.	Lat.	W. Long.
ISO (PHT-S)	1996-Dec-06	17:59:33	-2°	77°	12°	81°	-11°	76°	-18°	89°
ISO (SWS) start	1997-Sep-16	03:48	-41°	341°	-57°	334°	9°	316°	15°	301°
ISO (SWS) end	1997-Sep-16	07:16	-41°	296°	-57°	288°	9°	271°	15°	255°
MIDAS	2001-Oct-03	05:07	39°	296°	-48°	304°	-26°	325°	-30°	336°
MIDAS	2002-Sep-21	10:08	-14°	325°	-27°	323°	-5°	317°	0°	304°
MIDAS	2002-Sep-22	13:52	-14°	324°	-27°	322°	-5°	315°	0°	303°

Table 5: 22 Kalliope Sub-Earth and Sub-Solar Points

Observation Date	Time(UT)	Subsolar Point		Sub-Earth Point	
		Lat.	W. Long.	Lat.	W. Long.
2001-Oct-02	11:08-11:28	36°	225°-254°	14°	225°-255°
2001-Oct-02	12:30-13:02	36°	340°-24°	14°	340°-25°
2001-Oct-03	13:30-14:03	36°	350°-34°	14°	350°-35°

Figure 1: Reference Spectrum of the Calibration Star
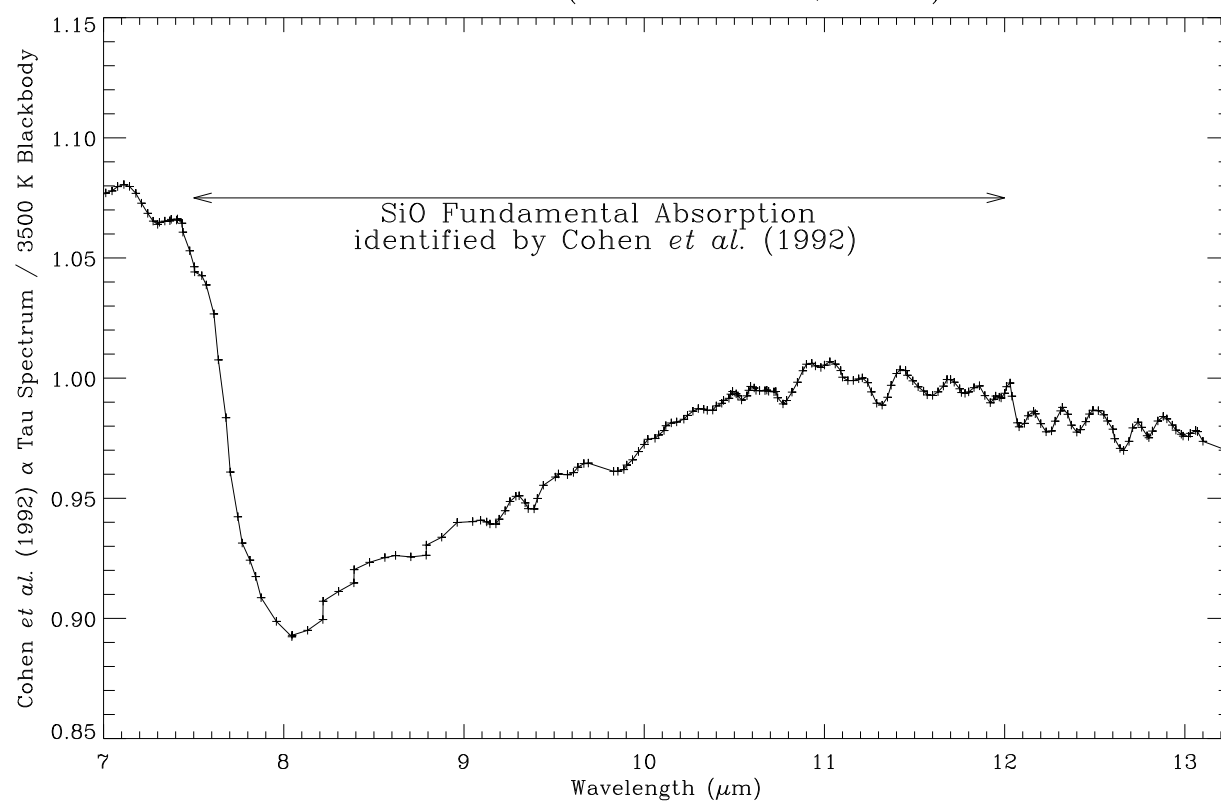α Tauri (Cohen *et al.*, 1992)
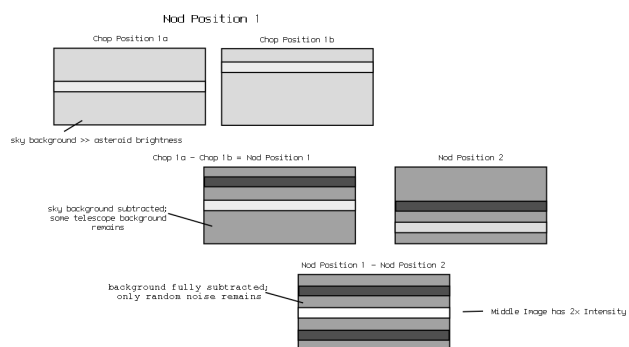
Figure 2a: On-Chip Chopping and Nodding

Nod Position 1

Chop Position 1a

Chop Position 1b

sky background >> asteroid brightness

Chop 1a - Chop 1b = Nod Position 1

Nod Position 2

sky background subtracted;
some telescope background
remains

Nod Position 1 - Nod Position 2

background fully subtracted;
only random noise remains

Middle Image has 2x Intensity

Figure 2b: Spatial Profile of an SC-10 Segment

Total Raw Signal Summed Over Columns

Detector Row Number
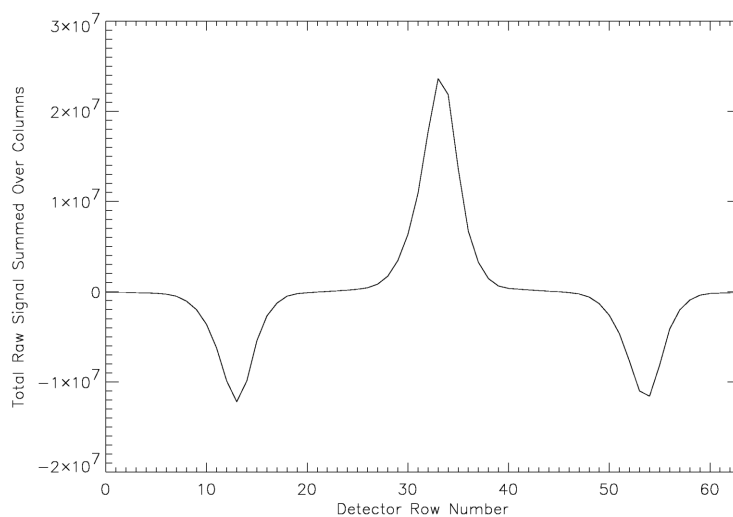
Figure 2c: Image of an SC-10 Segment

Rows

Columns

51
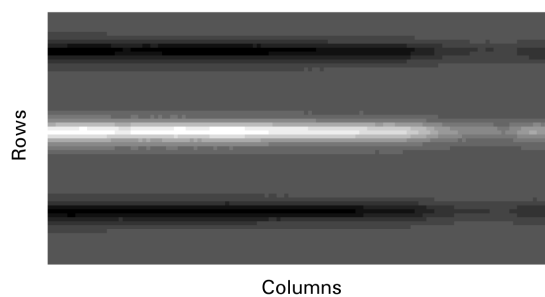
Figure 3: γ Aquilae Template and Data
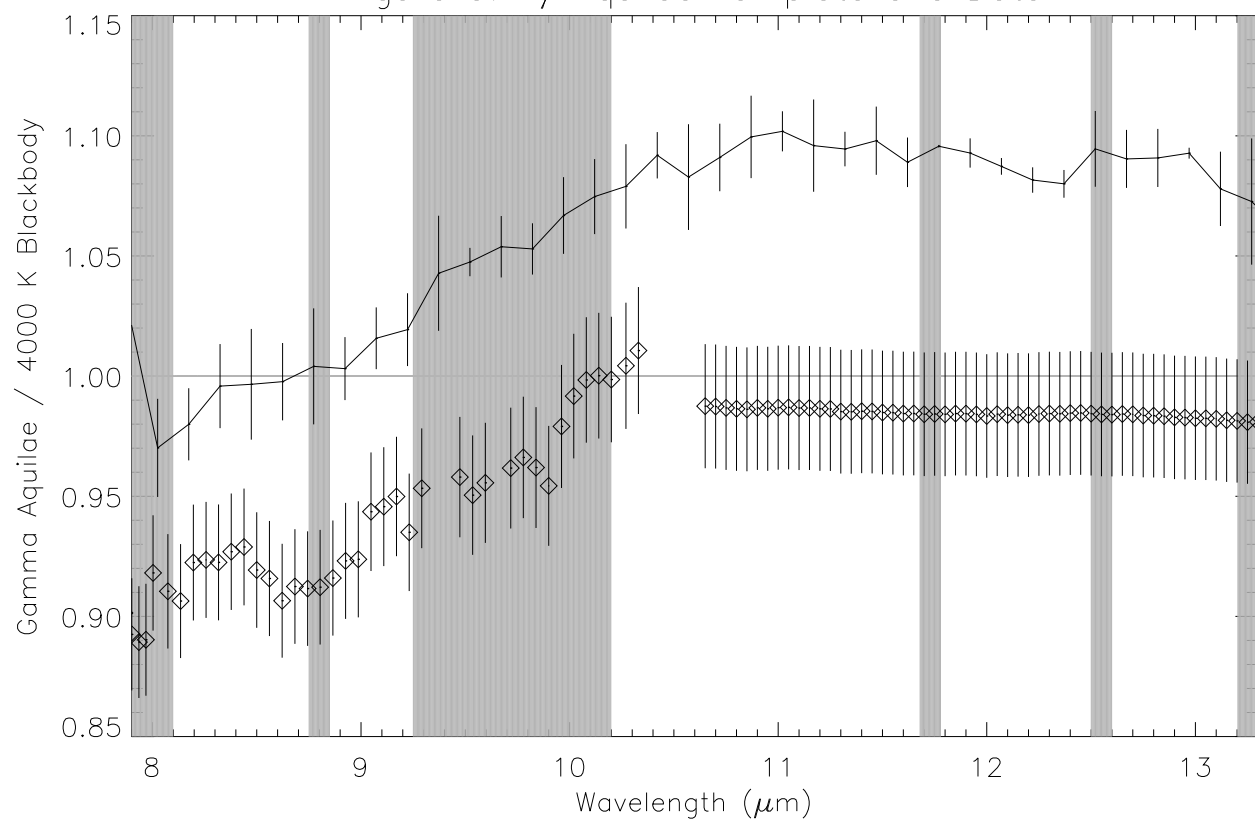
Figure 4: Model Atmospheric Transmission for Palomar Observatory
(ATRAN model, S.D. Lord, 1992)
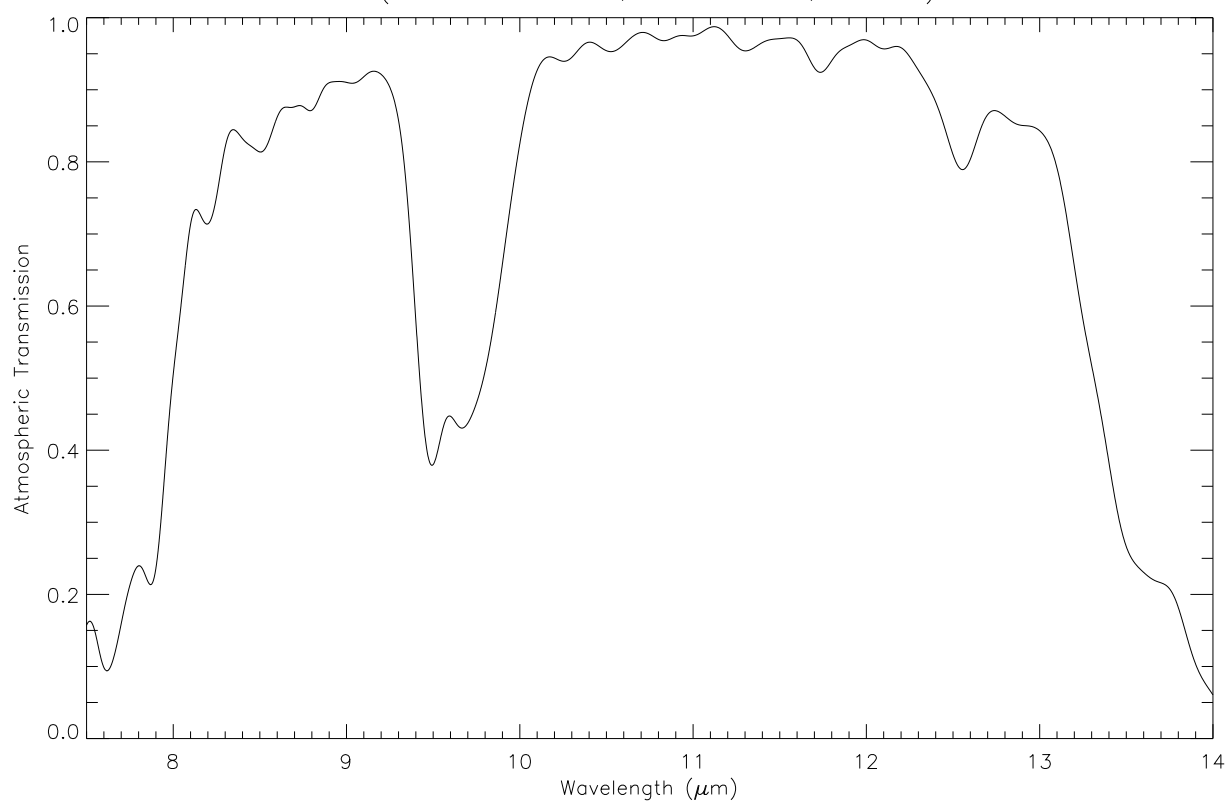
Figure 5: Wavelength Registration Artifacts
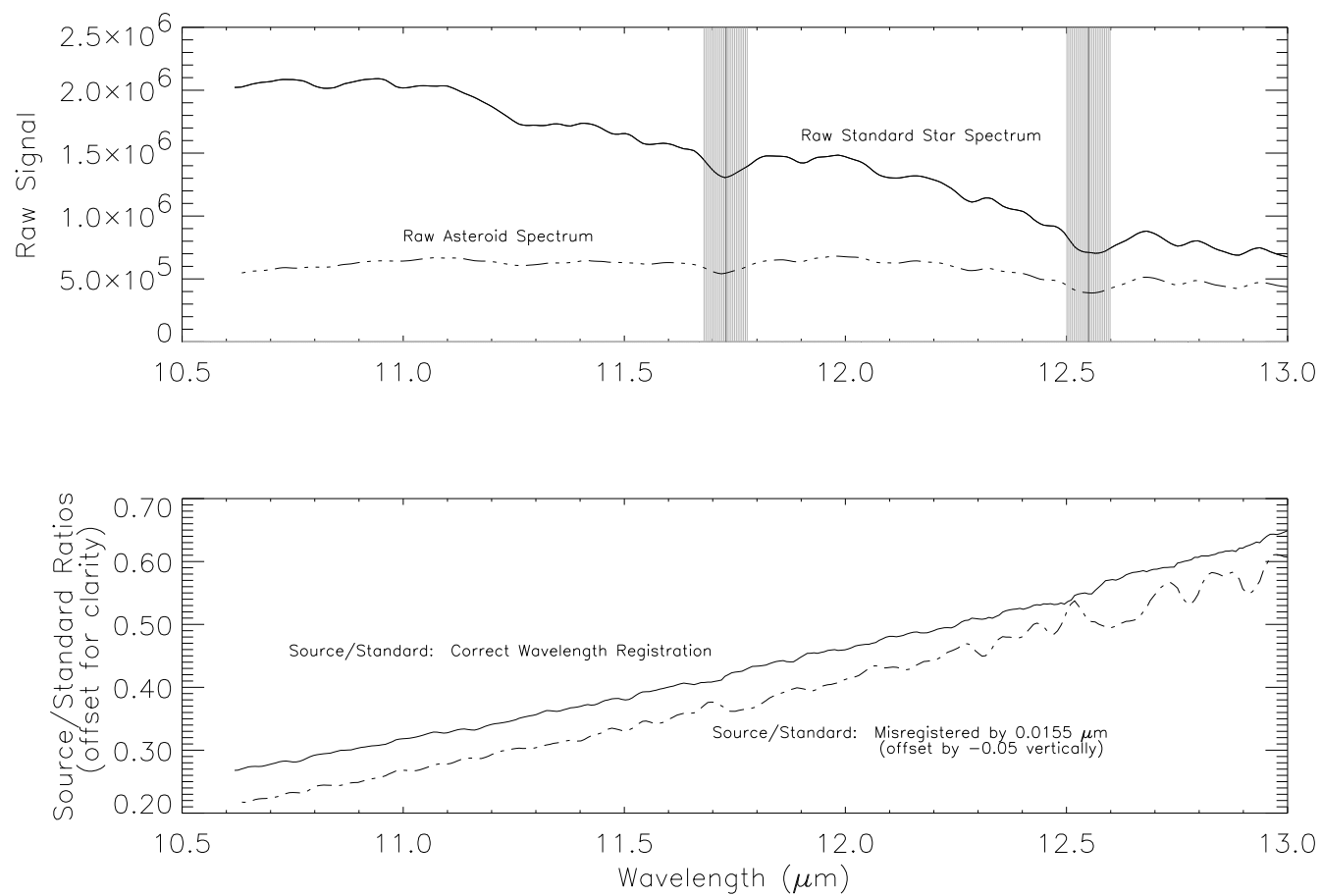
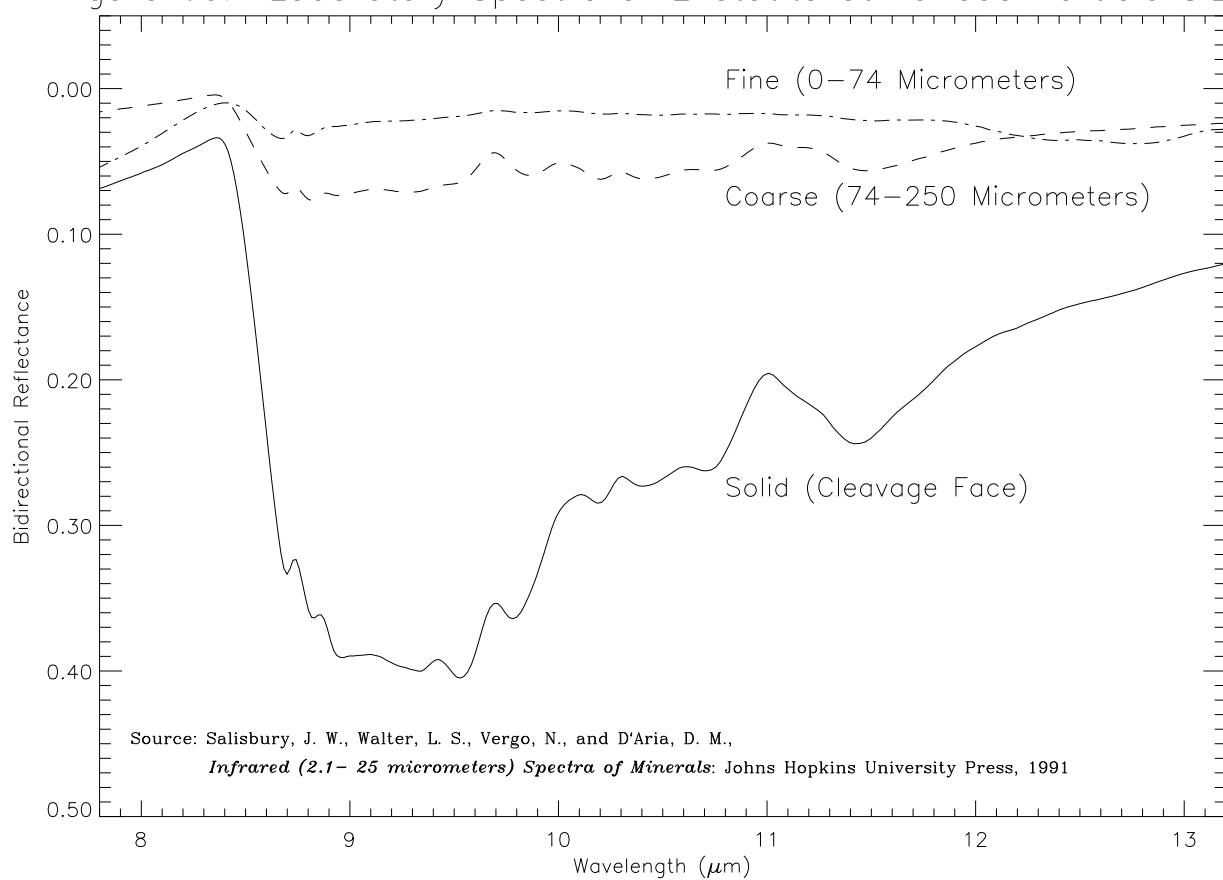Figure 6a: Laboratory Spectra of Enstatite at Various Particle Sizes

Fine (0–74 Micrometers)

Coarse (74–250 Micrometers)

Solid (Cleavage Face)

Bidirectional Reflectance

Wavelength (μm)

Source: Salisbury, J. W., Walter, L. S., Vergo, N., and D'Aria, D. M.,
Infrared (2.1– 25 micrometers) Spectra of Minerals: Johns Hopkins University Press, 1991

Figure 6b: Examples of Laboratory Spectra of Meteorite Samples at Fine (0−74 μm) Particle Sizes

La Criolla (L6)

Allende (CV3)

Johnstown (Diogenite)

Source: Salisbury, J. W., D'Aria, D. M., and Jarosewich, E.

"Midinfrared (2.5− 13.5 μm) Spectra of Powdered Stony Meteorites" *Icarus* 92, pp. 280−297, 1991.

Bidirectional Reflectance (offset by 0.015 for clarity)

Emissivity ~ 1 − 5·$r_{biconical}$

Wavelength (μm)
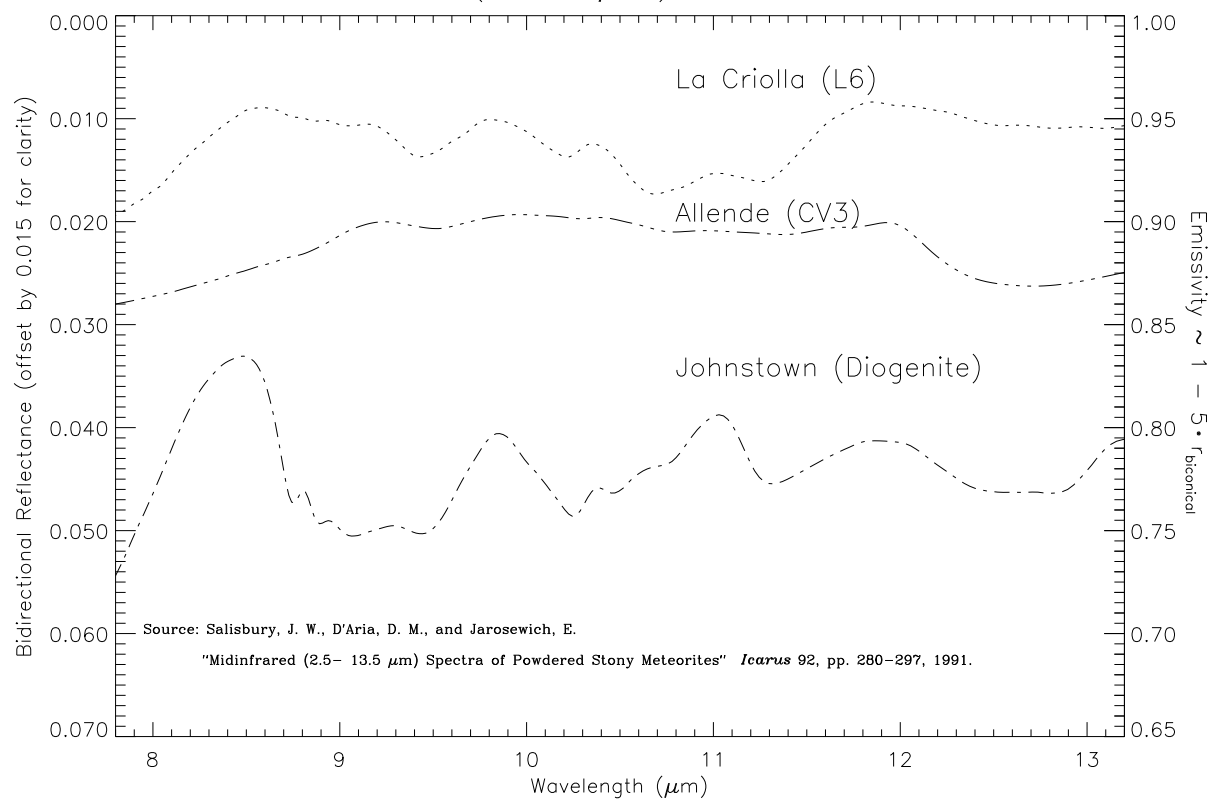
Figure 7: Flux Spectra of "MIDAS" Asteroids
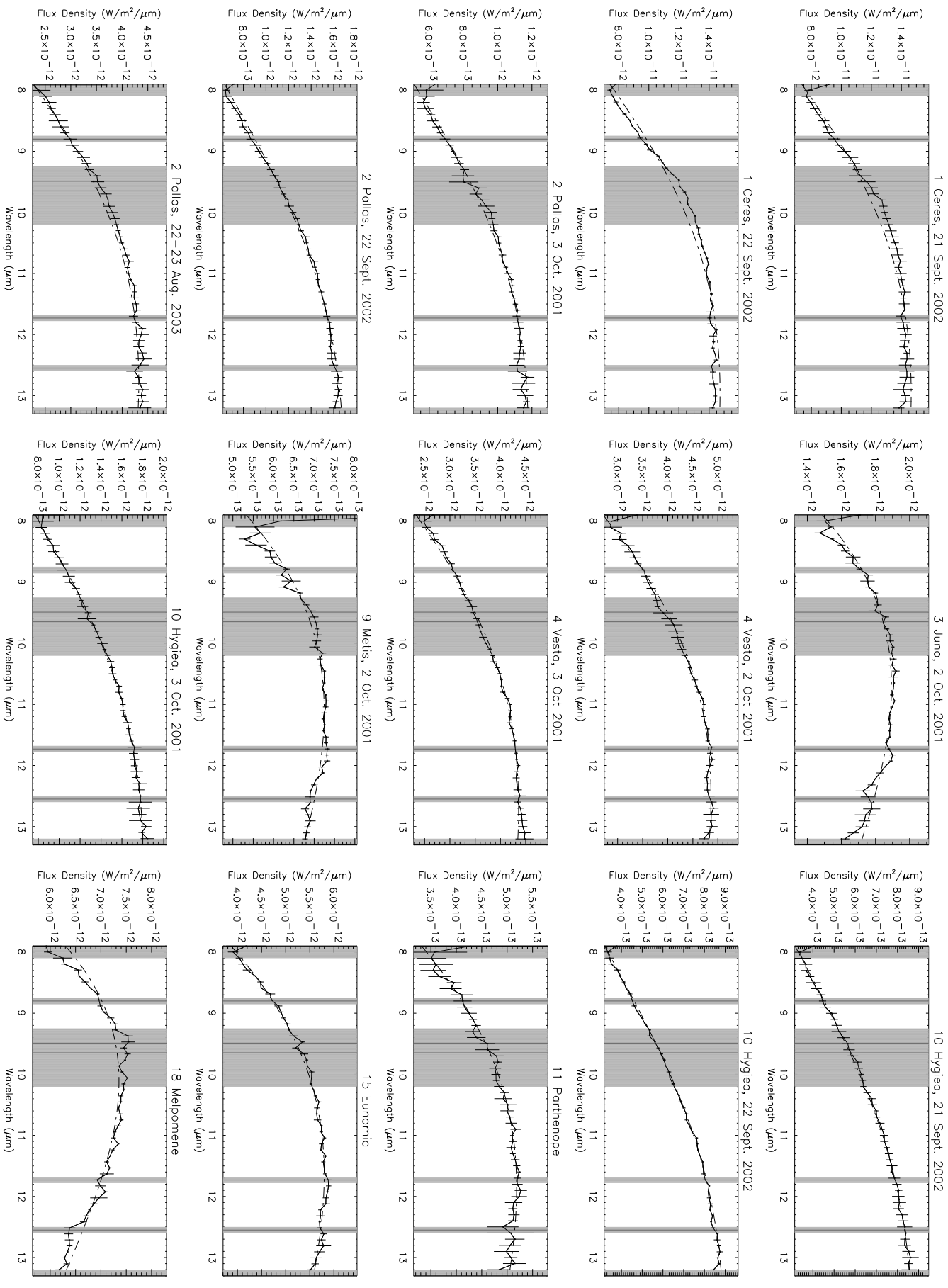
Figure 7, continued: Flux Spectra of "MIDAS" Asteroids
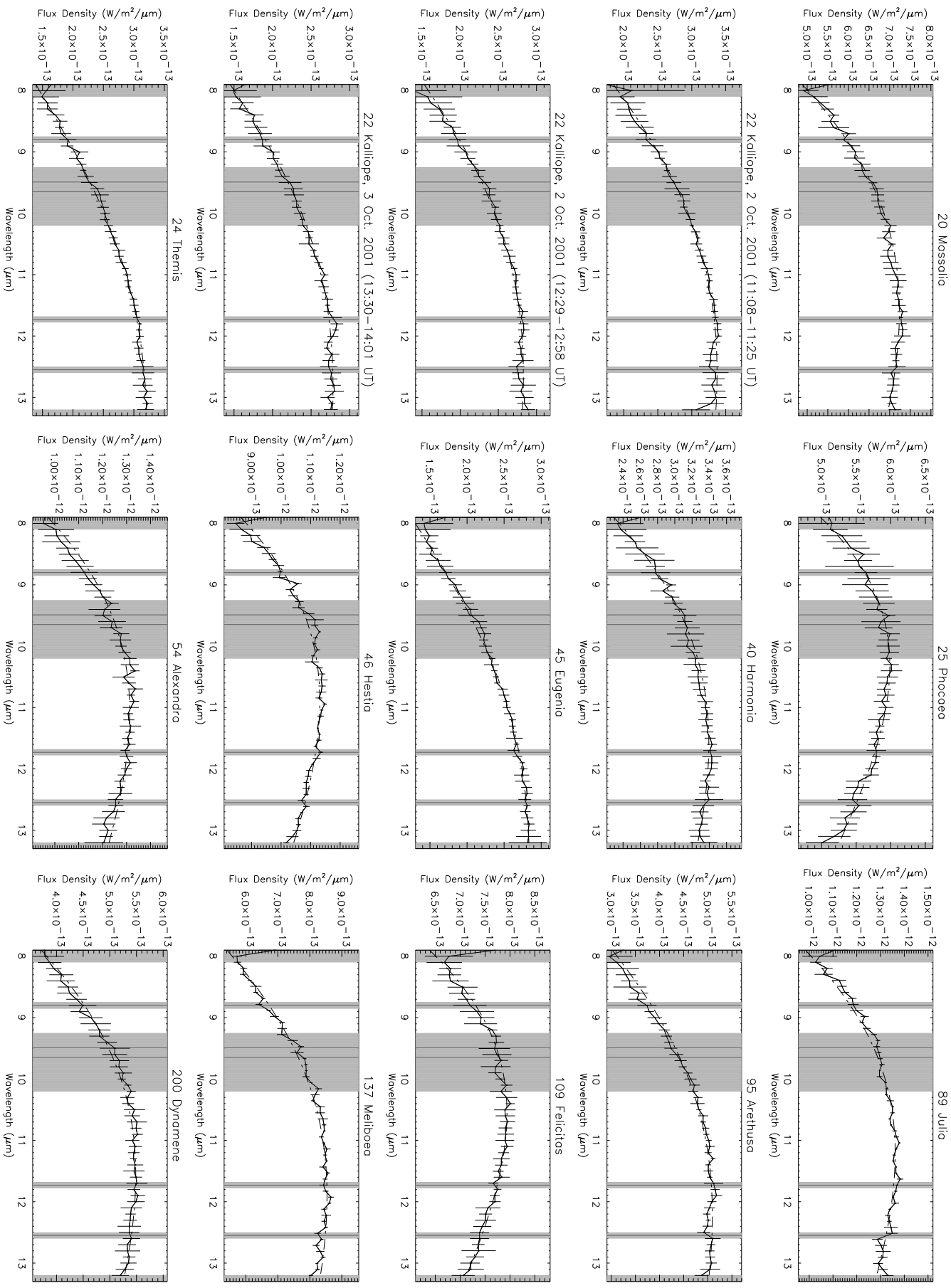
Figure 7, continued: Flux Spectra of "MIDAS" Asteroids

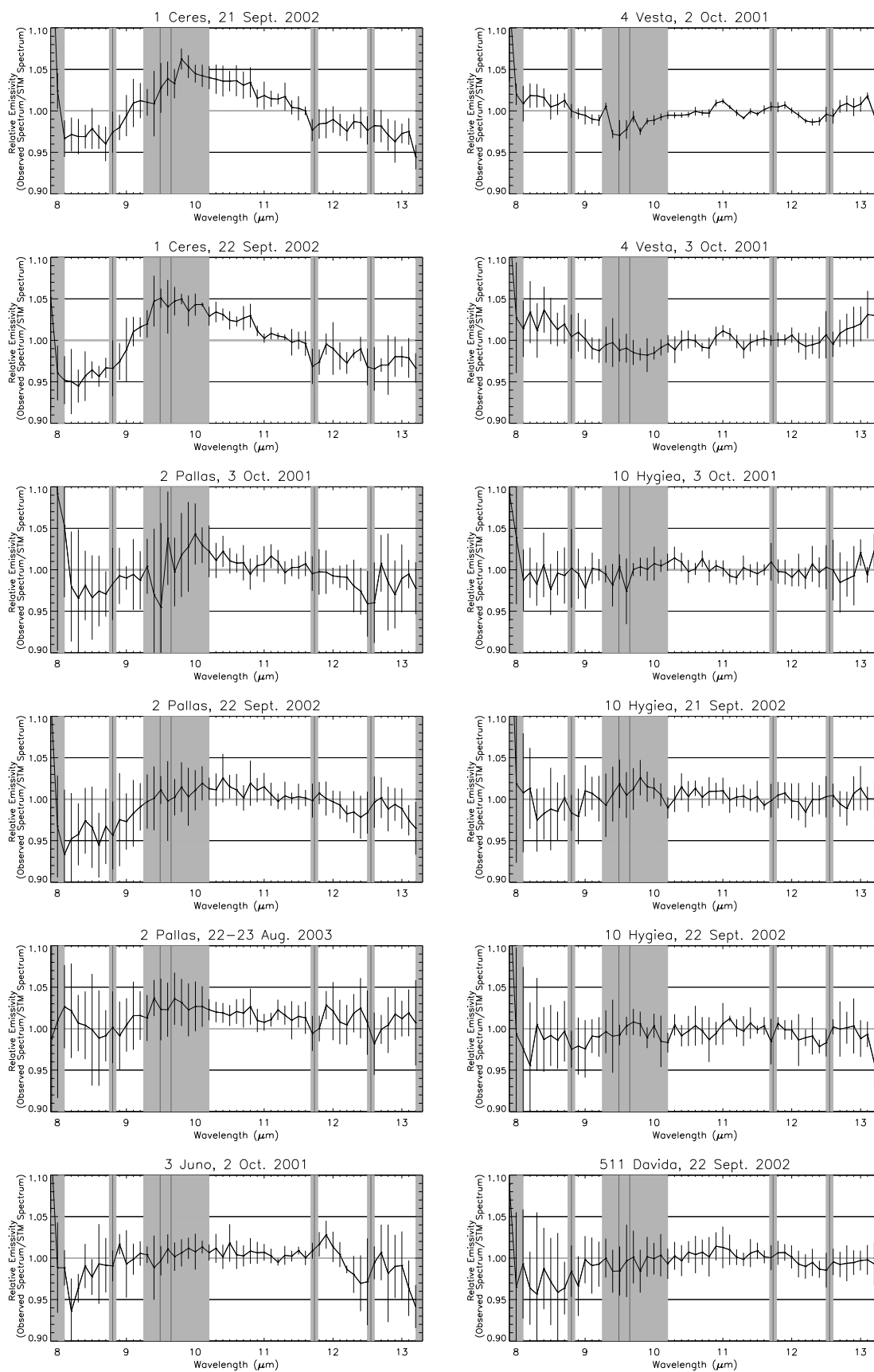# Figure 8: Emissivity Spectra of Selected Asteroids

1 Ceres, 21 Sept. 2002

4 Vesta, 2 Oct. 2001

1 Ceres, 22 Sept. 2002

4 Vesta, 3 Oct. 2001

2 Pallas, 3 Oct. 2001

10 Hygiea, 3 Oct. 2001

2 Pallas, 22 Sept. 2002

10 Hygiea, 21 Sept. 2002

2 Pallas, 22–23 Aug. 2003

10 Hygiea, 22 Sept. 2002

3 Juno, 2 Oct. 2001

511 Davida, 22 Sept. 2002
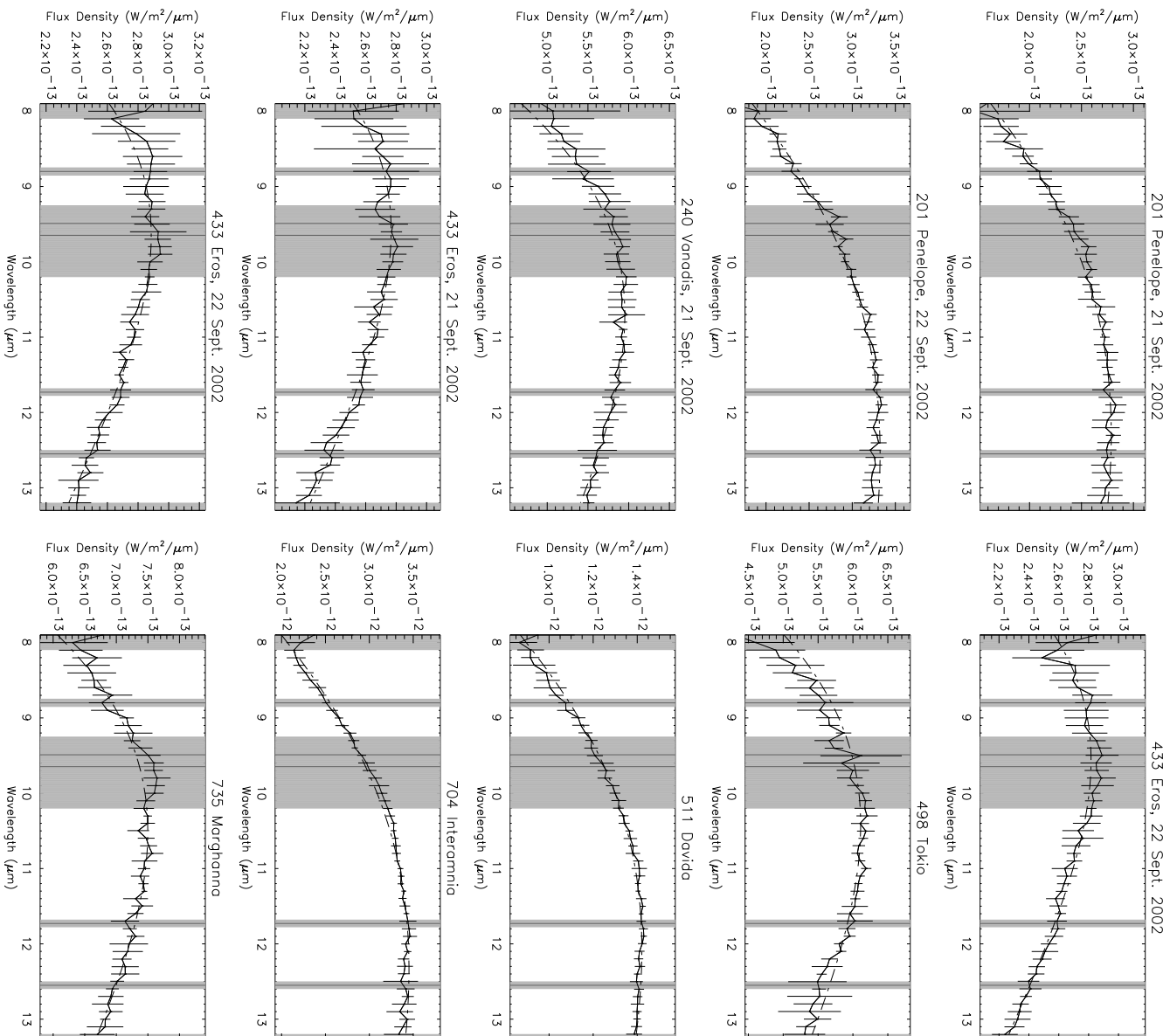
Figure 9: Thermal Infrared Spectra of 4 Vesta and Laboratory Materials

Vesta 2 Oct. 2001
Vesta 3 Oct. 2001
Yamato 791192 (Eucrite)
Johnstown (Diogenite)
Anorthite
Hypersthene (17 wt% FeO)

Relative Emissivity (offset for clarity)
Emiss. of Lab Materials ≈ 1 – 5•$r_{biconical}$

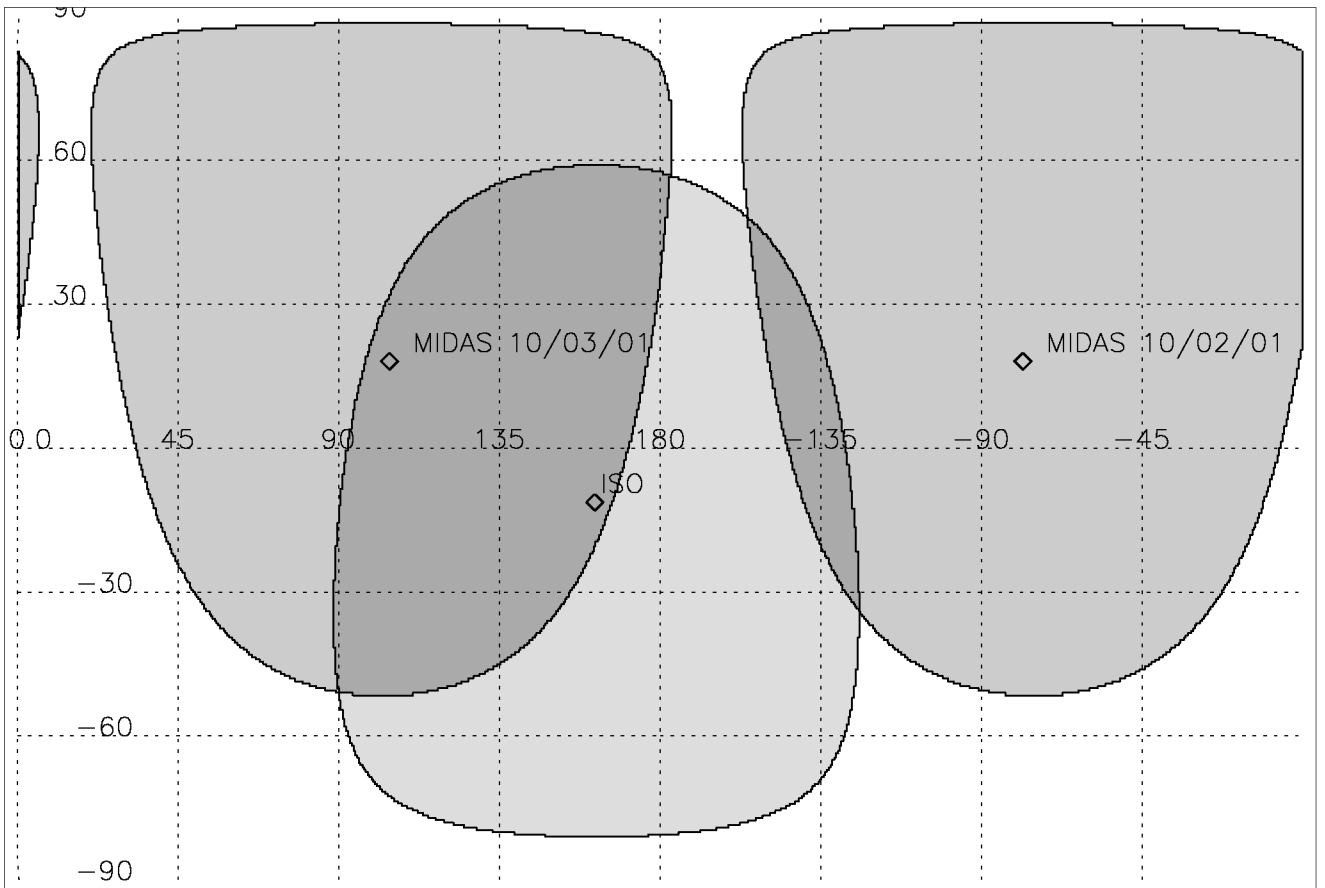Wavelength (μm)
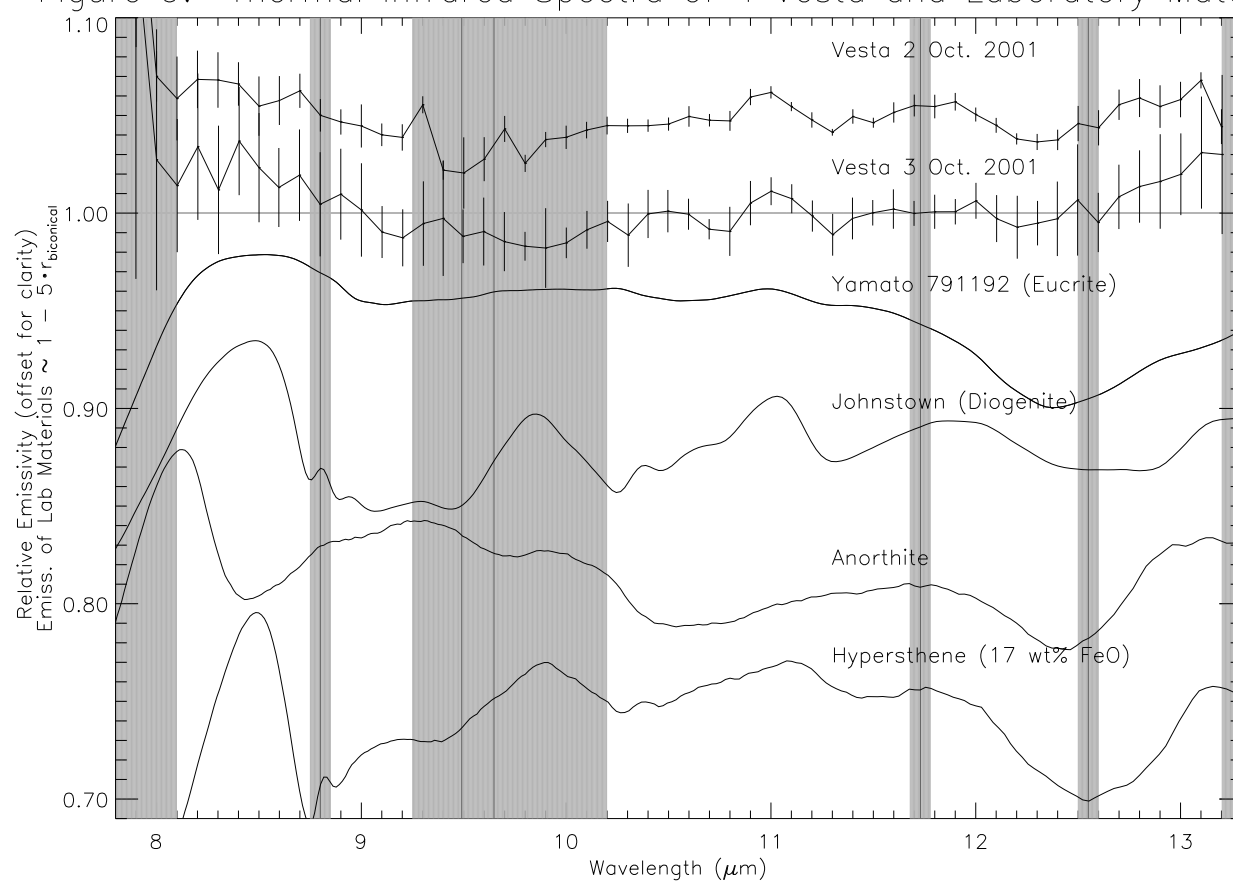
Figure 10: MIDAS and ISO fields of view for 4 Vesta

Figure 11a: MIDAS and ISO fields of view for 10 Hygiea
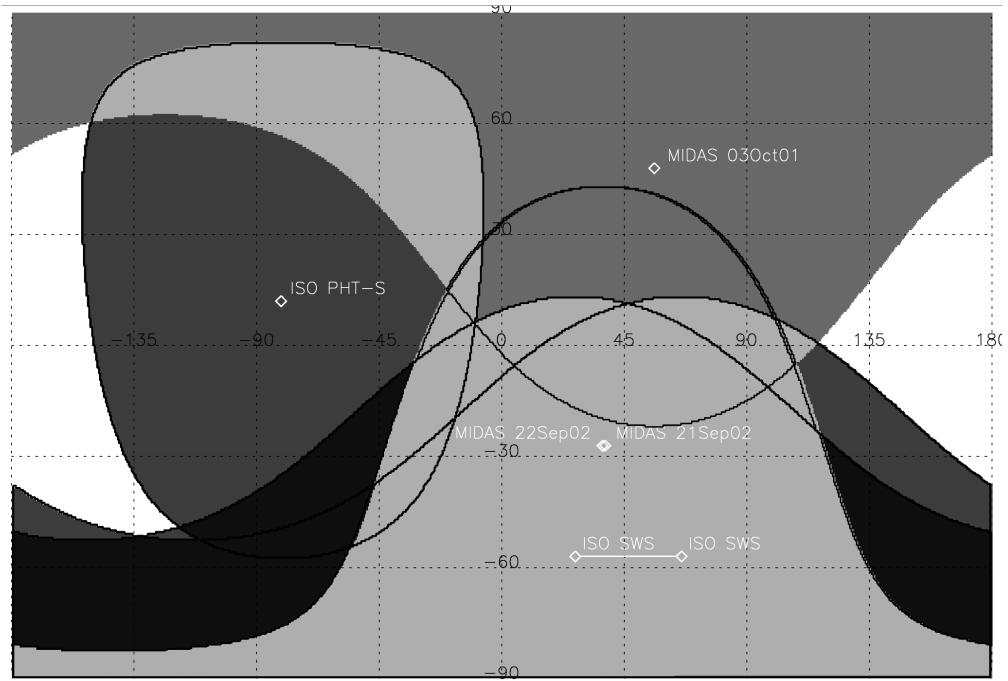"p3" pole solution ($\alpha = 120°$, $\delta = 34°$)

Figure 11b: MIDAS and ISO fields of view for 10 Hygiea
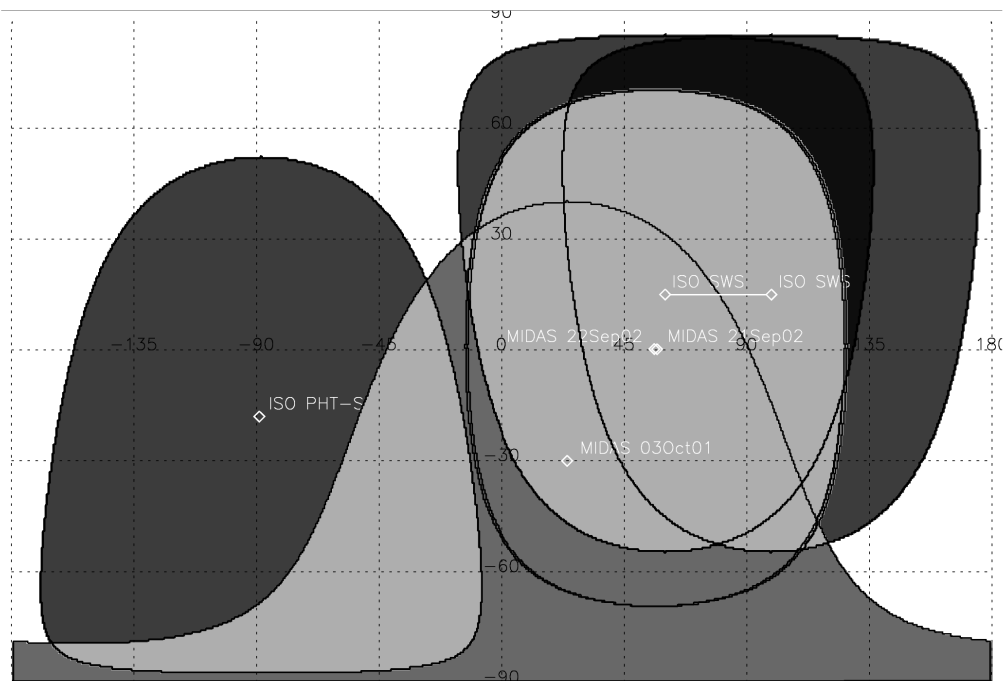"p4" pole solution: ($\alpha = 295°$, $\delta = 43°$)

Figure 12: Rotation Periods vs. Radii of MIDAS Asteroids With High and Low Values of η

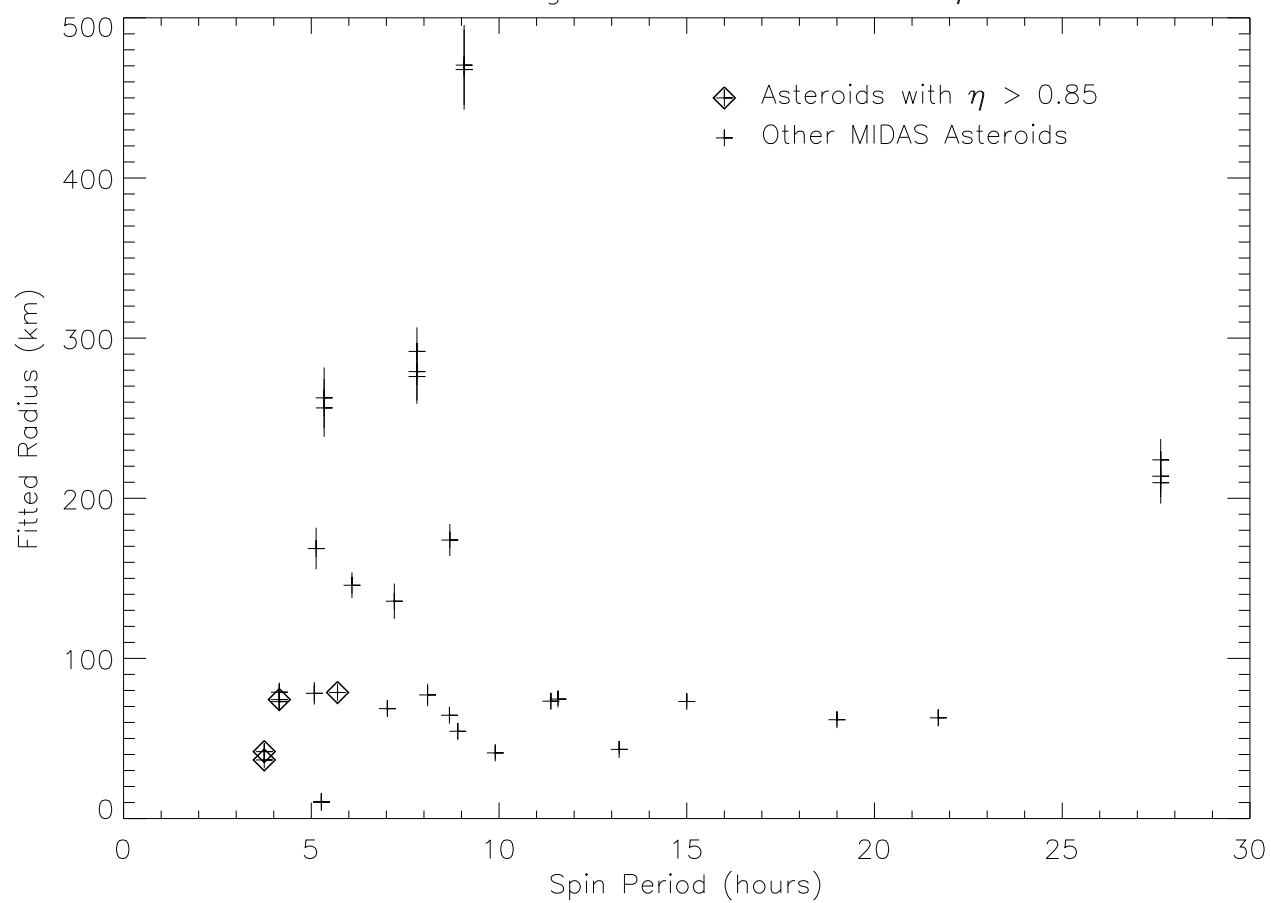Figure 13: MIDAS−derived Beaming Parameters (η) vs. Phase Angles